Atmospheric Research 345 (2027) 109391

Contents lists available at ScienceDirect

Atmospheric Research

journal homepage: www.elsevier.com/locate/atmosres

Evaluating the impact of aerosol treatments in TROPOMI NO_2 retrievals on top-down NO_x emission inversions over Eastern China

Wenhui Dong [a], Yi Wang [a,*], Yanyu Wang [b,*], Jiajun Xiong [a], Jintai Lin [c], Mengying Wang [c], Minghui Tao [a], Lunche Wang [a]

[a] Hubei Key Laboratory of Regional Ecology and Environmental Change, School of Geography and Information Engineering, China University of Geosciences, Wuhan, 430074, China
[b] State Environmental Protection Key Laboratory of Formation and Prevention of Urban Air Pollution Complex, Shanghai Academy of Environmental Sciences, Shanghai, 200233, China
[c] Laboratory for Climate and Ocean–Atmosphere Studies, Department of Atmospheric and Oceanic Sciences, School of Physics, Peking University, Beijing, 100871, China

ARTICLE INFO

Keywords:
NO_x emission inversion
GEOS-Chem adjoint
Data assimilation
TROPOMI NO_2

ABSTRACT

Accurate quantification of anthropogenic nitrogen oxides (NO_x) emissions is essential for understanding complex regional air pollution and evaluating emission reduction policies. Top-down inversion has become an important method for updating emission inventories; however, comprehensive assessments of how aerosol treatment differences in satellite inversion algorithms affect inferred emission estimates remain limited. This study utilized the GEOS-Chem adjoint model to assimilate both the operational Sentinel-5P/TROPOMI (S5P-OFFL) and Peking University POMINO NO_2 products to optimize anthropogenic NO_x emissions over eastern China in January and July 2023. The January VCD difference between POMINO and S5P-OFFL increased with aerosol optical depth ($R^2 = 0.51$), whereas no relationship occurred in July ($R^2 < 0.01$), indicating stronger aerosol-related retrieval effects in winter. Against MEIC-2023, the January S5P-OFFL inversion reduced the regional emission NMB to 30.2%, while POMINO preserved the grid-scale pattern more closely, increasing R from 0.67 to 0.80. In July, POMINO reduced the regional NMB by 18.7 percentage points to 10.0%, with similar spatial correlations for the two inversions. The POMINO-driven January posterior agreed more closely with OMI, achieving $R = 0.85$ and $NMB = -25.1\%$; the corresponding S5P-OFFL values were 0.81 and − 36.4%. POMINO also better reproduced winter NO_2 clustering. A common-weight sensitivity experiment reduced the positive emission adjustments in the POMINO inversion, demonstrating the influence of observation errors and regularization. Explicit aerosol treatment therefore preserved useful NO_2 information under high aerosol loading, while observation weighting, regularization, and model structure jointly controlled posterior emission magnitude.

1. Introduction

Nitrogen Oxides ($NO_x \equiv NO + NO_2$) are critical precursors to tropospheric ozone (O_3) and secondary fine particulate matter ($PM_{2.5}$), released from both anthropogenic sources such as fossil fuel combustion in transportation, industry, and power generation, and natural sources including soil microbial activity (Hudman et al., 2012; Liu et al., 2025). High concentrations of NO_2 and its secondary products pose a serious threat to public health and ecosystems (Xu et al., 2025). In response, China has implemented a series of stringent clean air policies over the past decade, leading to substantial emission reductions (Li et al., 2024; Xiong et al., 2026). However, the current air pollution regime in China is evolving into a more complex pattern, characterized by the coexistence of declining $PM_{2.5}$ and rising O_3 concentrations (Li et al., 2019), while frequent severe winter haze events remain a challenge for environmental governance. Concurrently, shifts in China's energy mix are changing the sectoral and regional patterns of fuel consumption, while the deployment of pollution-control technologies is reducing emission factors in major emitting sectors. Together, these processes are rapidly reshaping the magnitude and spatial distribution of anthropogenic NO_x emissions (Yang and Hong, 2023). Therefore, accurate quantification of NO_x emissions is essential for understanding the mechanisms of complex regional air pollution and for evaluating coordinated emission reduction strategies.

* Corresponding authors.
E-mail addresses: wangyi34@cug.edu.cn (Y. Wang), wangyy@saes.sh.cn (Y. Wang).

https://doi.org/10.1016/j.atmosres.2026.109391
Received 21 July 2026; Received in revised form 18 September 2026; Accepted 8 October 2026
Available online 13 October 2026
0169-8095/© 2026 Elsevier B.V. All rights are reserved, including those for text and data mining, AI training, and similar technologies.

Anthropogenic NO_x emissions have traditionally been quantified using bottom-up inventories based on energy consumption statistics and sector-specific emission factors. While fundamental for understanding source contributions, this approach suffers from inherent data reporting lags that fail to capture rapid, short-term emission changes (Feng et al., 2020). Furthermore, downscaling national or provincial emissions to gridded maps using proxies like population or Gross Domestic Product (GDP) introduces spatial allocation biases, often distorting local emission hotspots (Geng et al., 2017). To overcome these constraints, the scientific community has widely adopted top-down methods. Because freshly emitted NO is quickly converted to NO_2 in the atmosphere, satellite-observed NO_2 Vertical Column Density (VCD) serves as a robust spatial proxy for emission sources (Shah et al., 2023). In recent years, with the deployment of high-spatial-resolution instruments such as the TROPOspheric Monitoring Instrument (TROPOMI) and the utilization of data assimilation systems like four-dimensional variational (4D-Var) methods (Kong et al., 2025; Qu et al., 2019; Wang et al., 2020), top-down inversions have become a core approach for correcting biases in emission inventories (Duncan et al., 2016; Ye et al., 2026) and tracking fine-scale emission trends (Cooper et al., 2017).

However, the reliability of these top-down estimates depends largely on the accuracy of the underlying satellite retrieval products. Driven by the fine spatial resolution of recent sensors like TROPOMI, the primary limitation has shifted from spatial coverage to retrieval accuracy (Goldberg et al., 2021; Kim et al., 2016). Instead, systematic biases inherent in the retrieval algorithms themselves, particularly in the calculation of the Air Mass Factor (AMF), have emerged as the new bottleneck for accurate emission constraints. The differences in how various retrieval algorithms treat high aerosol loading are particularly critical. The official standard TROPOMI product typically adopts an implicit aerosol correction scheme, treating aerosols as an effective cloud layer (van Geffen et al., 2022b). While this simplification is globally effective, it introduces substantial systematic biases over regions with frequent severe winter haze, such as China, where aerosol scattering and absorption can severely alter the effective optical path length, leading the official product to significantly underestimate NO_2 column densities in heavily polluted areas (Lin et al., 2014). In contrast, the Peking University Ozone Monitoring Instrument NO_2 (POMINO) algorithm explicitly incorporates aerosol optical properties into radiative transfer calculations, which effectively mitigates the common underestimation of NO_2 observed in standard products over highly polluted regions and recovers the true NO_2 signals under severe haze conditions (Lin et al., 2015; Liu et al., 2020).

These systematic differences arising from the retrieval algorithms inevitably propagate into the data assimilation framework, altering the estimated emissions (Miyazaki et al., 2012). Such observation heterogeneities across distinct satellite products persist across various spatial scales and pollution regimes. On a global scale, analysis-observation differences exhibit structural discrepancies in spatial distribution when assimilating different sensors such as OMI, SCIAMACHY, and GOME-2 (Miyazaki et al., 2017). Systematic observational differences between OMI-QA4ECV v1.1 product and TROPOMI v1.2 beta product induce a ~ 15% uncertainty in global posterior NO_x emissions and affect the numerical simulation of secondary tropospheric ozone through photochemical feedbacks (Sekiya et al., 2022). In regional high-resolution applications under relatively clean backgrounds like Europe, assimilating OMI-QA4ECV v1.1 versus TROPOMI-RPRO v02.04 yields divergent estimates for the 2005–2019 NO_x anthropogenic emission reductions (16% vs. 45%, respectively), with the inversion performance showing sensitivity to the specification of super-observation errors and weights (Fortems-Cheiney et al., 2025). By comparing NO_2-constrained inversions based on the Tropospheric Emissions Monitoring of Pollution (TEMPO) version 3 level-2 product and the TROPOMI offline (OFFL) level-2 product, Hsu et al. (2026) demonstrated that differences in satellite sampling and product-specific biases can propagate into top-down NO_x emission estimates.

These prior investigations have illustrated the implications of cross-sensor discrepancies, and evaluations remain limited to comparisons between different satellite platforms. In heavy-pollution regions like China, Kong et al. (2022) demonstrated that utilizing the TROPOMI-POMINO product successfully identified numerous small-to-medium anthropogenic sources and transportation emissions that were ambiguous or missing in traditional bottom-up inventories, underscoring the region-specific suitability of aerosol-corrected products. The effective use of satellite NO_2 observations in emission inversions also depends on how the observations are processed and weighted, including spatial aggregation and the characterization of observation uncertainties (Plauchu et al., 2024; Rijsdijk et al., 2025). Although previous studies have demonstrated the superiority of explicit aerosol correction at the satellite retrieval level (Lin et al., 2015; Liu et al., 2020), systematic and quantitative evaluations of how different TROPOMI retrieval products perform within numerical model assimilation systems remain limited. Specifically, how the observational discrepancies introduced by these two fundamentally different aerosol treatment schemes propagate through complex non-linear chemical mechanisms to affect posterior emission estimates, and how these schemes improve the simulation of near-surface NO_2 concentrations, remain critical questions to be elucidated.

To address this, we employ the GEOS-Chem adjoint model to construct a regional data assimilation system, independently assimilating the Sentinel-5P/TROPOMI level 2 NO_2 products and POMINO NO_2 products. Selecting January 2023 (characterized by high winter aerosol loading) and July 2023 (representing clean summer conditions) as typical scenarios, we comprehensively evaluate and compare the performance of different satellite retrieval algorithms in constraining anthropogenic NO_x emissions and improving the representation of spatial pollution gradients. This aims to provide a reliable scientific basis for regional air quality forecasting and targeted emission control strategies. The remainder of this paper is organized as follows. Section 2 details the configuration of the GEOS-Chem adjoint model, the implementation of the custom nested domain, and the specific retrieval methodologies of the operational Sentinel-5P/TROPOMI and POMINO products. Section 3 contrasts the differences in the top-down emission estimates driven by the two assimilation scenarios. Section 4 evaluates the impacts of these optimized emissions on posterior NO_2 simulations and their spatial structures. Section 5 presents episodic case studies to further elucidate assimilation performance under severe haze versus clean atmospheric conditions. Finally, Section 6 summarizes the main findings.

2. Methodology and datasets

2.1. The GEOS-Chem model and its adjoint

The three-dimensional chemical transport model GEOS-Chem and its adjoint (v35n) are applied to simulate atmospheric NO_2 and to optimize anthropogenic NO_x emissions (Henze et al., 2007; Henze et al., 2009). As the forward model in the assimilation system, GEOS-Chem simulates atmospheric composition from local to global scales (Long et al., 2015). Meteorological fields from the NASA Global Modeling and Assimilation Office (GMAO) Forward Processing system (GEOS-FP) are used to drive the simulations (Lucchesi, 2013). Key physical processes include convective transport (Putman and Lin, 2007), advection (Lin and Rood, 1996), deposition (Liu et al., 2001), and boundary-layer mixing (Lin and McElroy, 2010). A detailed tropospheric gas-phase chemical mechanism is implemented in GEOS-Chem to explicitly represent the coupled O_3–NO_x–VOC photochemical system, capturing radical-driven oxidation pathways that regulate ozone chemistry, reactive nitrogen speciation, and the production of key secondary pollutants (Wang et al., 1998). In addition to gas-phase photochemistry, GEOS-Chem simulates heterogeneous reactions on aerosols (Kasibhatla et al., 2018), including N_2O_5 hydrolysis, halogen activation, and the uptake of reactive nitrogen and

sulfur species. Collectively, these processes enable physically and chemically consistent simulations of tropospheric oxidant budgets, reactive nitrogen cycling, and the formation of secondary air pollutants on regional to global scales.

Anthropogenic emissions are derived from the Hemispheric Transport of Air Pollution inventory (HTAP v2.2), provided as monthly gridded data at a horizontal resolution of 0.1° × 0.1° (Janssens-Maenhout et al., 2015). Over the Asian region, this dataset is consistent with the MIX (Model Inter-Comparison Study for Asia) emission inventory (Li et al., 2017b). In this study, we refer to the MIX inventory used here as MIX-2010. The 2010 emissions were not extrapolated to 2023 because they served as the a-priori state of the inversion rather than as an estimate of the actual emissions in 2023. Spatially resolved emission scaling factors were optimized by balancing the mismatch between the simulated and observed 2023 TROPOMI NO_2 slant columns against the departure from the prior emissions. Therefore, the posterior emissions were allowed to depart from the 2010 baseline according to the satellite constraints, although some dependence on the older prior may remain in regions with relatively weak observational constraints or strong regularization. Biogenic emissions are calculated using the Model of Emissions of Gases and Aerosols from Nature (MEGAN) (Guenther et al., 2012). Natural sources of NO_x are represented using a combination of inventories and parameterization schemes: biomass burning emissions are derived from the Global Fire Emissions Database (GFED, version 3) (van der Werf et al., 2017); soil NO_x emissions are calculated following the parameterization of Hudman et al. (2012); lightning NO_x emissions are simulated using a cloud-top-height-based parameterization constrained by satellite observations (Murray et al., 2012; Ott et al., 2010).

To focus on eastern China, the high-resolution GEOS-Chem adjoint simulation is performed over a custom nested domain spanning 110°E ~ 123.125°E and 20.25°N ~ 42.75°N at a horizontal resolution of 0.25° × 0.3125°. The inversion analysis targets January and July 2023. Lateral boundary conditions are provided by a global simulation at 2° × 2.5° resolution. Meteorological fields (GEOS-FP), emission inventories, and initial conditions are aligned to the nested domain. A six-month spin-up run was conducted before the study period to minimize the influence of initial chemical fields.

The GEOS-Chem adjoint model utilizes the backward chain rule to efficiently compute the gradient of a predefined cost function with respect to all control variables (Henze et al., 2007; Henze et al., 2009). An observation operator for TROPOMI NO_2 was developed and validated in this study (for details, see Text S1). The observation operator maps the simulated NO_2 fields from the model space to the TROPOMI observational space. To validate this application, the numerical correctness of the operator was verified by comparing adjoint gradients against finite-difference approximations (Fig. S1). The consistency between the two approaches confirms the mathematical integrity of the framework.

2.2. *TROPOMI NO_2 satellite retrieval product*

TROPOMI instrument aboard the European Space Agency's (ESA) Copernicus Sentinel-5 Precursor (S5P) satellite provides the tropospheric NO_2 observations used in this study (Veefkind et al., 2012). Launched in October 2017, S5P operates in a solar-synchronous polar orbit with an afternoon overpass at approximately 13:30 local time and a swath width of up to 2600 km. This mission provides daily global coverage of atmospheric composition at an unprecedented spatial resolution of 5.5 km × 3.5 km (after August 2019), enabling the detection of localized emission plumes from individual power plants, industrial parks, and urban centers (Prunet et al., 2020).

Retrieval of tropospheric NO_2 column density begins with processing TROPOMI Level 1b reflectance spectra. Level-2 NO_2 product is generated using the retrieval algorithm described by van Geffen et al. (2022b), with further technical details provided in the corresponding algorithm theoretical basis document (van Geffen et al., 2022a). Differential Optical Absorption Spectroscopy (DOAS) compares satellite-measured radiances with solar irradiance spectra (Lange et al., 2023) and fits laboratory-measured NO_2 absorption cross sections at specific temperatures to retrieve the integrated concentration along the effective optical path, referred to as the total Slant Column Density (SCD). Subsequently, a Stratosphere-Troposphere Separation (STS) step is performed to isolate the tropospheric component (Veefkind et al., 2012). The official TROPOMI retrieval algorithm typically employs a data assimilation scheme based on the TM5-MP chemical transport model. The initially retrieved total NO_2 column is assimilated into the model, which leverages its representation of stratospheric chemistry and global circulation to estimate the stratospheric background field. The stratospheric component is then subtracted from the total SCD to derive the tropospheric SCD. The final step converts the observation-geometry-dependent tropospheric SCD to the tropospheric VCD using the AMF, which quantifies the vertical sensitivity of the satellite observation and depends on a-priori information (Boersma et al., 2011). The tropospheric level 2 NO_2 VCD data are obtained by dividing the tropospheric SCD by the AMF. To ensure high data quality, we apply stringent filtering criteria, retaining only pixels with a quality assurance (QA) value >0.75. This filtering removes pixels affected by cloud contamination or unfavorable viewing geometry, thereby enhancing the robustness and reliability of the analysis. Because the POMINO-TROPOMI products provide neither an independently calculated quality control variable nor an observation-time variable, each POMINO file is linked to the corresponding operational TROPOMI file using the acquisition date and orbit number retained in its filename. The POMINO grid cells are then spatially matched to the operational product, and only those corresponding to operational TROPOMI observations with QA > 0.75 are retained. Thus, the QA value is not recomputed for POMINO but is applied as a common screening criterion for the two products.

A prominent source of uncertainty in the tropospheric NO_2 VCD retrieval stems from the AMF used to convert the slant columns to vertical. This is particularly evident over heavily polluted regions such as eastern China, where inversion accuracy is strongly influenced by the AMF calculation (Liu et al., 2020). In high aerosol-load environments, the presence and vertical distribution of aerosols can alter the original effective optical path, leading to systematic biases in the retrieved NO_2 tropospheric VCD (Chimot et al., 2019). To rigorously assess how these retrieval algorithms affect top-down estimates, we compared the performance of two widely used products in constraining anthropogenic NO_x emissions: the official operational Sentinel-5P/TROPOMI product (S5P-OFFL) which is provided by European Union's Copernicus Programme and the ESA, and Peking University's POMINO v2 product (Liu et al., 2020) which is based on TROPOMI offline v2.4.0 data. The analysis focuses on January and July 2023, representing typical winter and summer conditions, to evaluate the seasonal variability of the retrieval impacts. POMINO-TROPOMI v2 is publicly available beginning in January 2023; therefore, 2023 is the earliest complete calendar year for which this specific version can be compared with the corresponding operational S5P-OFFL product.

The important distinction between the official S5P-OFFL and the POMINO retrieval algorithm lies in their treatment of aerosols and surface reflectance. The official NO_2 retrieval algorithm developed by Royal Netherlands Meteorological Institute (KNMI) and used to generate the S5P-OFFL product represents aerosol effects implicitly through the effective cloud model, in which aerosol-induced radiative effects may be incorporated into retrieved cloud parameters such as cloud fraction and cloud pressure. This implicit treatment can lead to biased estimates of the optical path length, particularly during periods of severe air pollution. In such conditions, aerosols will be erroneously identified as high-altitude clouds. This misclassification distorts the calculated optical path lengths, typically resulting in a shielding effect where the reduced sensitivity to boundary-layer NO_2 is not adequately represented in the

AMF calculation, potentially resulting in an overestimated AMF and an underestimated tropospheric NO_2 column. In contrast, the POMINO algorithm employs an explicit aerosol correction framework (Lin et al., 2015; Lin et al., 2014). By integrating daily Aerosol Optical Depth (AOD) from Moderate Resolution Imaging Spectroradiometer (MODIS) and vertical profiles from the GEOS-Chem model, POMINO utilizes the Linearized Discrete Ordinate Radiative Transfer (LIDORT) model to precisely calculate aerosol scattering and absorption processes. Furthermore, POMINO employs Bidirectional Reflectance Distribution Function (BRDF) coefficients provided by MODIS to describe the anisotropic characteristics of surface reflectance, thereby replacing the directional Lambertian reflection used in the official retrieval algorithm. As a result, this explicit treatment of aerosol radiation interactions reduces the underestimation of tropospheric NO_2 in regions with severe air pollution (Liu et al., 2020). To account for inherent discrepancies between the prior profiles in retrievals and simulated by GEOS-Chem, the model profiles are convoluted with the satellite averaging kernels and air mass factors to ensure a physically consistent comparison. Full description of the linear interpolation of scattering weights and the mathematical formulations is detailed in the Text S2.

2.3. Independent validation data

To objectively evaluate the performance of the two TROPOMI NO_2 retrieval algorithms in constraining anthropogenic emissions and improving NO_2 simulations, we performed cross-validation using multiple independent observational datasets and emission inventories. These datasets include ground-based in situ observations, independent satellite remote sensing products, and high-resolution NO_x emission inventories.

2.3.1. Surface observations

The National Real-Time Urban Air Quality Release Platform established by the China National Environmental Monitoring Center (CNEMC) provides surface NO_2 concentration and Air Quality Index (AQI) data (Wang et al., 2014). This monitoring network covers major Chinese cities, employing the standard chemiluminescence method for continuous sampling and monitoring of near-surface NO_2 concentration. We collected hourly observation data from 1282 stations within the study area, and these in-situ measurements served as ground-based reference for validating the spatial distribution of near-surface NO_2 concentrations simulated by the assimilated model. Daily average AQI data are used to supplement the representation of air pollution levels in the case study (detailed in Section 5).

2.3.2. OMI tropospheric NO_2 column product

In addition to TROPOMI observations, this study incorporates tropospheric NO_2 columns from the NASA standard Aura/Ozone Monitoring Instrument (OMI) Level-2 product (OMNO2 Collection 3, version 4.0). The retrieval framework is described in the OMI Algorithm Theoretical Basis Document (ATBD) (Boersma et al., 2002), with the version 4.0 updates by Lamsal et al. (2021). OMI also operates in a solar-synchronous orbit with afternoon overpasses (approximately 13:30 local time). Its extensive observation sequence (from 2004 to present) provides a crucial reference for assessing the consistency of simulated posterior NO_2 VCD. Although OMI spatial resolution (13 km × 24 km) is coarser than TROPOMI, its long-term, sensor-independent record enables an unbiased evaluation of systematic biases in simulated NO_2 column density after TROPOMI NO_2 assimilation, reducing the risk of product-specific circular validation.

2.3.3. MODIS MAIAC AOD product

To quantitatively assess the potential impact of aerosol on NO_2 inversion and assimilation, this study employs the MODIS MAIAC (Multi-Angle Implementation of Atmospheric Correction) AOD product (Lyapustin et al., 2011). This product integrates observations from both Terra and Aqua satellites, providing aerosol depth data with spatial resolution as high as 1 km using a multi-angle atmospheric correction algorithm. AOD data are employed to analyze whether and where tropospheric NO_2 columns and aerosol loading exhibit spatial co-location and how such associations vary between seasons in specific air quality case studies, particularly when evaluating the physical mechanism underlying improvements in assimilation results achieved using the POMINO algorithm with explicit aerosol correction.

2.3.4. MEIC v2.0 emissions inventory

The China Multi-Scale Emission Inventory Model v2.0 (MEIC v2.0), developed by Tsinghua University (Li et al., 2017a), was selected as the underlying baseline for comparison. MEIC v2.0 integrates China's socioeconomic statistics from 1990 to 2023, pollution source census data, and sectoral emission factors, providing high-precision anthropogenic emission estimates with a spatial resolution of 0.25° × 0.25°. This inventory covers core sectors including power, industry, residential, agriculture, and transportation. Its bottom-up NO_x emission serves as a reference for evaluating the accuracy of top-down emissions derived from satellite assimilation in this study. By comparing the spatial distribution difference between optimized emissions and the underlying MEIC inventory in key urban clusters, the corrective capabilities of the two TROPOMI NO_2 algorithm products on the spatiotemporal distribution of the prior inventory can be revealed.

2.4. Data assimilation framework and optimization strategy

We constrain anthropogenic NO_x emissions using 4D-Var framework based on the adjoint method, defining unitless emission scaling factor ($\boldsymbol{\sigma}$) as the control variable. Within each grid cell (i,j), the relationship between the posterior emission E and the prior emission E_a is expressed as:

$$\sigma(i,j) = \frac{E(i,j)}{E_a(i,j)} \tag{1}$$

At the initial stage, the prior scaling factor is initialized as a vector of one.

The objective of the inversion system is to iteratively minimize the cost function J, thereby seeking the optimal balance between emission estimates of scaling factors and observational constraints alongside prior knowledge. The mathematical form of the cost function is as follows:

$$J(\boldsymbol{\sigma}) = J_{\text{obs}} + \gamma J_{\text{prior}} \tag{2}$$

$$J_{\text{obs}} = \frac{1}{2}\sum_{t\in\Omega}(H(\boldsymbol{c}) - \boldsymbol{s})^T \mathbf{S}_{\text{obs}}{}^{-1}(H(\boldsymbol{c}) - \boldsymbol{s}) \tag{3}$$

$$J_{\text{prior}} = \frac{1}{2}(\boldsymbol{\sigma} - \boldsymbol{\sigma}_a)^T \mathbf{S}_{\text{prior}}{}^{-1}(\boldsymbol{\sigma} - \boldsymbol{\sigma}_a) \tag{4}$$

Where, Prior term (J_{prior}) measures the deviation of prior parameter ($\boldsymbol{\sigma}_a$) from control variable ($\boldsymbol{\sigma}$), reflecting the extent to which inversion result is constrained by the prior inventory. The observation operator (H) maps the GEOS-Chem simulated NO_2 concentration ($\boldsymbol{c}$) field onto the slant column of satellite observation, eliminating implicit reliance on the satellite's prior profile. Observation term (J_{obs}) measures residuals between model-simulated values ($H(\boldsymbol{c})$) and TROPOMI satellite observation ($\boldsymbol{s}$) in the slant column space. Ω is the available spatiotemporal domain of the observation data. Gradients of the cost function with respect to the emission scaling factors are calculated via backward integration of the GEOS-Chem adjoint model, and the minimization is performed iteratively until convergence.

The prior error matrix ($\mathbf{S}_{\text{prior}}$) reflects the uncertainty in the prior inventory. Following assessments of anthropogenic NO_x emissions over Asia (Lu et al., 2024; Qu et al., 2017), we set the prior uncertainty for each grid cell to 50%. The observation error matrix ($\mathbf{S}_{\text{obs}}$) is set as a diagonal matrix. Its elements encompass the absolute measurement

error of the satellite instrument, retrieval error, and model characterization error. To mitigate interference from noise below the satellite detection threshold, we set the error for the S5P-OFFL simulation based on the tropospheric NO_2 precision of the S5P-OFFL NO_2 product. Since the POMINO NO_2 data product does not directly provide a precision field, we calculated the NO_2 standard deviation measured over the ocean far from continental land. We considered the NO_2 observed in these areas to originate from instrument observation errors (Boersma et al., 2004). However, this ocean-based estimate does not represent total POMINO retrieval uncertainty and does not include structural uncertainty in the AMF calculation.

The regularization parameter (γ) is used to adjust the relative weight between observation constraints and prior terms. The choice of γ determines the balance between fitting the satellite observations and adhering to the a-priori information. The L-curve method (Hansen, 2000) is employed to determine its optimal value. By varying the magnitude of γ across a series of independent inversion trials, we plot the response curves of J_{obs} versus J_{prior}. The γ value corresponding to the point of maximum curvature on the curve is selected as the baseline (Fig. S2). For another month, γ is dynamically scaled based on the ratio of the actual number of effective observations relative to the baseline month to ensure physical consistency in inversion strength across months.

3. NO_x emission inversions constrained by different satellite products

3.1. Evaluation of satellite NO_2 columns and observational uncertainties

The S5P-OFFL and POMINO TROPOMI NO_2 products exhibit consistent spatial coverage and valid observation counts across both January and July 2023 (Fig. 1c, d, i, j). Despite this consistency in data sampling, their tropospheric VCD diverges. Over major anthropogenic source regions, specifically the North China Plain (NCP), Yangtze River Delta (YRD), and Pearl River Delta (PRD) (Detailed geographic partitions and province locations can be viewed in Fig. 2), the NO_2 VCD from the POMINO algorithm framework is notably higher than the results from the S5P-OFFL official algorithm products (Fig. 1a, b, g, h). This enhancement is observable in both seasons but is particularly pronounced during winter.

Another factor governing their performance in the assimilation system is their observation error. The S5P-OFFL product provides pixel-specific inversion uncertainty, and the spatial errors generated show high values in the North China region. The POMINO observation error is empirically defined as the standard deviation of monthly mean VCD over clean, remote ocean grids. As shown in the error histograms (Fig. 1f, l), this static POMINO baseline (3.66×10^{14} and 5.08×10^{14} molecules/cm^2 for January and July, respectively; red dashed lines) falls below the bulk of the S5P-OFFL error distribution.

To further evaluate the spatial and sub-regional variations between the two satellite products, a cross-sectional transect line passing through Shijiazhuang, Beijing, and the rural sectors of Hebei province is analyzed (Fig. 2). In both winter and summer 2023, systematically higher tropospheric NO_2 VCD are observed for the POMINO compared to the S5P-OFFL product within the core urban segments. Over the urban grids of Shijiazhuang and Beijing, the absolute numerical difference between the two products ranges from approximately 0.2×10^{16} to 0.5×10^{16} molecules/cm^2. Conversely, over the sparsely populated rural regions of Hebei where anthropogenic activities are limited, the VCD derived from both algorithms exhibits close numerical convergence with minimal deviations. The standard deviations, shown as shaded envelopes around the monthly means, describe the dispersion of the

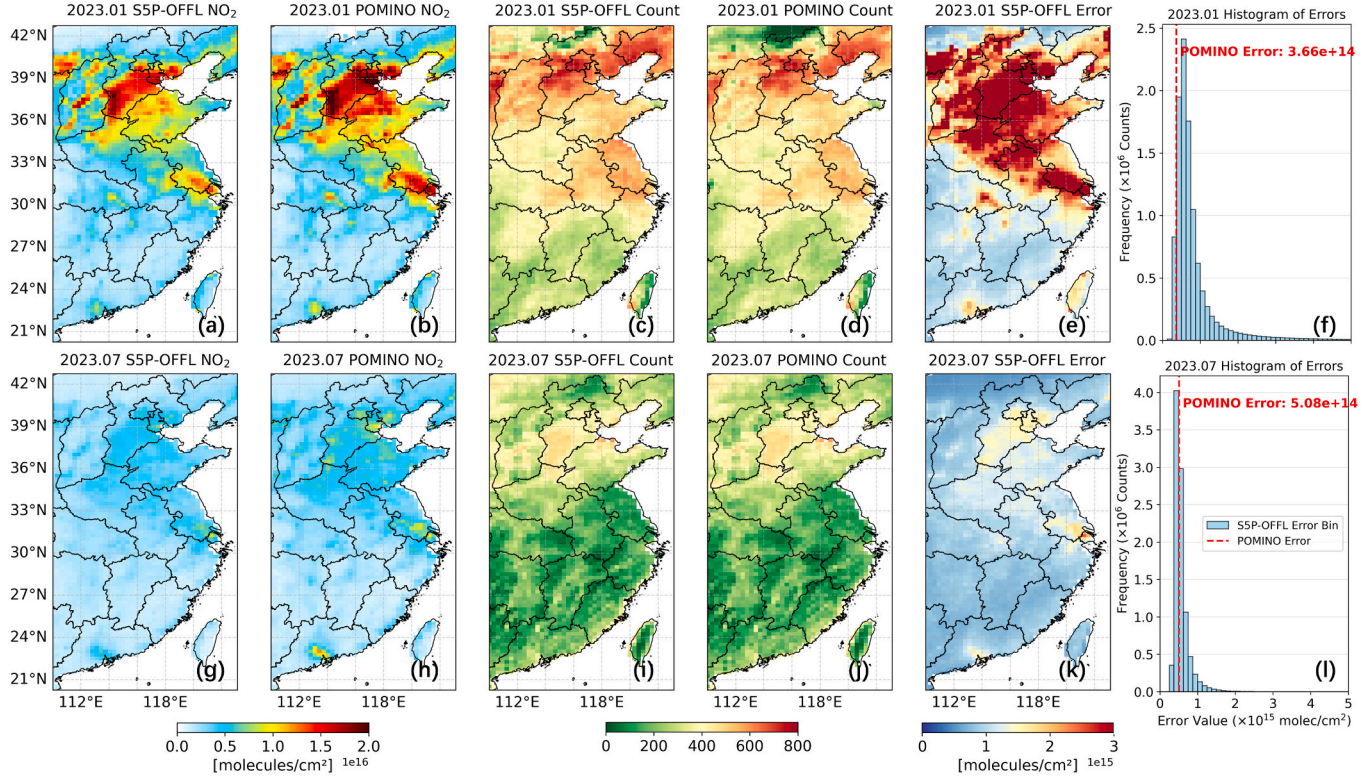


Fig. 1. Comparison of TROPOMI tropospheric NO_2 vertical column densities, valid observation counts, and observation errors between the S5P-OFFL and POMINO products. The top row shows S5P-OFFL NO_2 VCDs (a), POMINO NO_2 VCDs (b), valid S5P-OFFL observation count (c), valid POMINO observation count (d), S5P-OFFL observation errors (e), and S5P-OFFL error histogram (f) in January 2023. The bottom row (g-l) is similar to the top row, but for July 2023. In the histograms (f, l), the red vertical dashed lines denote the uniform regional observation error baseline applied to the POMINO product (3.66×10^{14} molecules/cm^2 for January and 5.08×10^{14} molecules/cm^2 for July). (For interpretation of the references to colour in this figure legend, the reader is referred to the web version of this article.)

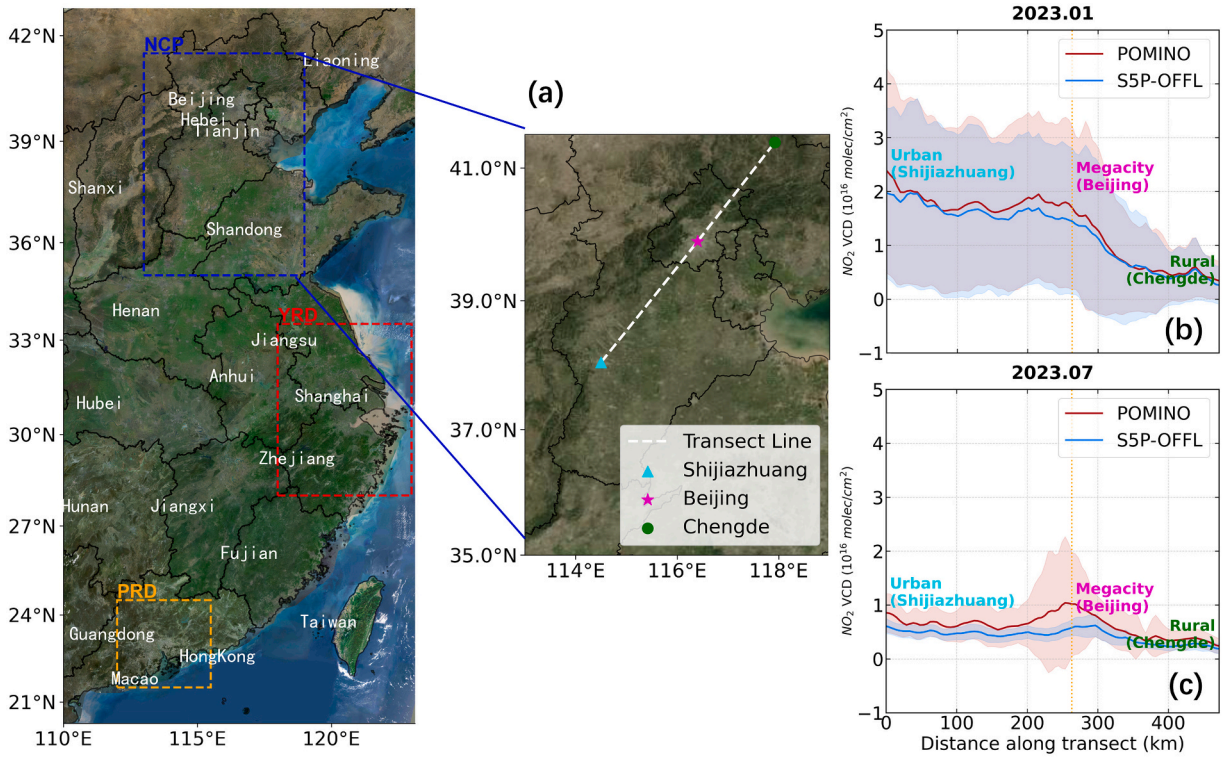


Fig. 2. Geographic domain definitions and cross-sectional variations of tropospheric NO_2 VCD across the NCP. (a) Spatial extents of primary anthropogenic source regions over Eastern China (NCP in blue, YRD in red, and PRD in orange dashed boxes) alongside the zoomed-in map of the NCP highlighting the cross-sectional transect path (white dashed line) that sequentially connects Shijiazhuang (urban city, cyan triangle), Beijing (megacity, magenta star), and Chengde (rural site, green circle). Spatial variations of tropospheric NO_2 VCD along the defined southwest-to-northeast transect are presented for (b) January 2023 and (c) July 2023, comparing the POMINO (red lines) and S5P-OFFL (blue lines) products. The shaded envelopes represent ±1 standard deviation around the mean, calculated from all retained retrieval pixels within each 0.1° grid cell during the month and subsequently interpolated along the transect. The vertical orange dotted line marks the geographic location of Beijing. (For interpretation of the references to colour in this figure legend, the reader is referred to the web version of this article.)

retrieval pixels contributing to each monthly grid-cell mean and display clear seasonal differences along the transect. During July, the standard deviation of the POMINO product is found to be larger than that of S5P-OFFL along the urban corridors. This divergence in data variability is most prominent in the vicinity of the megacity Beijing, where the monthly mean standard deviation of POMINO exceeds that of S5P-OFFL by a factor of over 5. These localized and season-dependent variations indicate that the discrepancies between POMINO and S5P-OFFL are not spatially uniform and reflect the combined effects of multiple inputs to the AMF calculation, including aerosol representation, surface reflectance, cloud parameters, and a priori NO_2 profiles.

With the objective of tracing the systematic discrepancies in tropospheric NO_2 VCD and evaluating their structural uncertainties, the differences (POMINO minus S5P-OFFL) in AMF and effective cloud fraction (CF) were analyzed using pixel-level spatial matching (Fig. 3). In January 2023, a pronounced north-south contrast is observed across Eastern China. Over the NCP, ΔAMF ranges from −0.4 to −0.1, accompanied by a systematically negative ΔCF (approximately −0.05 to 0). This spatial covariation is consistent with the high wintertime aerosol loadings typical of northern China (Chimot et al., 2016; Liu et al., 2020). POMINO's explicit aerosol correction partitions a portion of the scattering signal from the cloud retrieval into the aerosol module, resulting in a lower effective CF relative to the official FRESCO cloud product. Over southern China, particularly Hunan and Jiangxi provinces, ΔAMF exhibits positive values exceeding 0.4, with ΔCF showing a weakly positive anomaly. This feature likely reflects the combined influence of complex topography, surface BRDF effects, and low-level cloud configurations (Lorente et al., 2017).

The spatial difference patterns undergo substantial seasonal modifications in summer. Over the NCP, the negative ΔAMF intensities are enhanced, while ΔCF remains slightly negative across the region. This persistence indicates that the aerosol-related signal in the POMINO cloud correction continues to influence the retrieval during summer, albeit with a reduced magnitude. In southern China, the ΔCF field transitions to a widely distributed but weakly positive pattern (0 to 0.05), and the ΔAMF mosaic pattern becomes more moderate under cleaner background conditions.

Given that the S5P-OFFL and POMINO frameworks utilize the same level-1 satellite spectra, their retrieved tropospheric SCDs are virtually identical. Consequently, any divergence in the final tropospheric VCD arises from the mathematical and physical formulations of the AMF calculation. The a-priori NO_2 profiles constitute an important input to the AMF calculation, and the VCD-based comparisons in this section therefore retain their influence. In contrast, the subsequent emission inversion is conducted in tropospheric SCD space using product-specific scattering weights and GEOS-Chem NO_2 profiles and is therefore independent of the a-priori NO_2 profiles adopted in the satellite VCD retrievals, as described in Section 2.4 and Text S2. By calculating the absolute difference ($\Delta VCD = VCD_{POMINO} - VCD_{S5P\text{-}OFFL}$), a signal governed by algorithm-specific AMF processing is left. As illustrated in Fig. 4, the relationship between ΔVCD and AOD exhibits distinct patterns between the two seasons. In January, although the highest point density occurs at relatively low AOD, the distribution spans a broader range and contains more samples with AOD > 0.5 than in July. This indicates that high aerosol loadings in January occur within a smaller subset of the matched samples rather than representing the dominant condition across the NCP. Nevertheless, a clear positive relationship is observed over the full AOD range, with a regression slope of 0.45 and an R^2 of 0.51. At low aerosol loadings, the bin-averaged ΔVCD approaches zero, indicating consistent AMF derivations between the implicit and

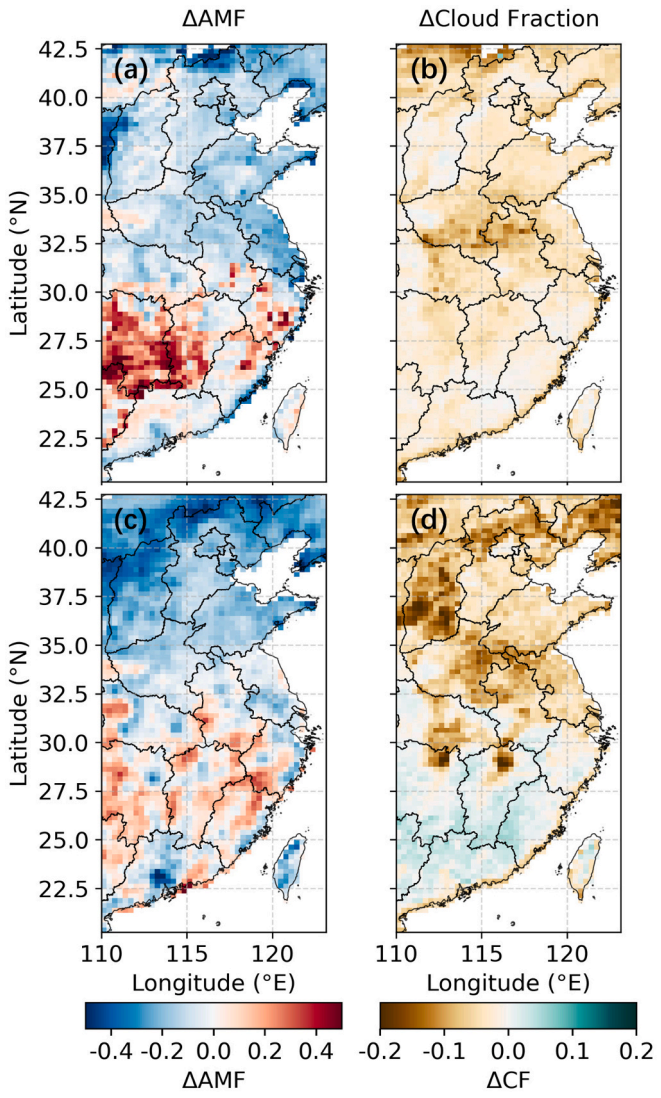


Fig. 3. Spatial distributions of the differences (POMINO minus S5P-OFFL) in key retrieval parameters for tropospheric NO_2 over Eastern China for January 2023 (top row: a, b) and July 2023 (bottom row: c, d). Panels from left to right denote the discrepancies in the air mass factor (ΔAMF), and effective cloud fraction (ΔCF). Both parameters were computed using quality-controlled, pixel-level matched retrievals to ensure comparability.

explicit algorithms under clean atmospheric conditions. As AOD increases toward 1.0, the bin-averaged ΔVCD continuously increases, exceeding 0.4×10^{16} molecules cm^{-2}. In July, the samples are more densely concentrated at moderate AOD, but ΔVCD shows no systematic dependence on AOD ($R^2 < 0.01$).

3.2. *Quantitative assessment and attribution of top-down NO_x inversions*

The assimilation of S5P-OFFL and POMINO tropospheric NO_2 products into the GEOS-Chem adjoint framework yields distinct spatiotemporal adjustments to the anthropogenic NO_x emissions across Eastern China for January and July 2023 (Fig. 5). In January, the S5P-OFFL-constrained inversion (Fig. 5a) produces a comparatively widespread reduction over the major source regions of eastern China, particularly across the North China Plain (NCP). The POMINO-constrained inversion is more spatially heterogeneous, combining downward adjustments over parts of eastern China with localized positive increments over the southern NCP and surrounding regions (Fig. 5b). Some of these increments exceed 50–100% relative to MIX-2010, and the resulting emissions in parts of northern China exceed not only MEIC-2023 but also the MIX-2010 prior. In July, both inversions predominantly reduce emissions relative to the prior (Fig. 5c, d). Overall, the contrast between the two inversions is more pronounced in January but remains evident in July.

Driven by the optimization framework, both product-based inversions exhibit a widespread downward revision of emissions relative to the prior MIX-2010 inventory (Fig. 6c, g, d, h). The independent comparison between MIX-2010 and MEIC-2023 indicates domain-wide emission decreases of approximately 44.2% in January and 44.5% in July (Fig. S7). This generalized reduction over Eastern China quantitatively reflects the significant decadal emission mitigation achieved through China's clean air policies implemented between 2010 and 2023, correcting the substantial baseline overestimation introduced by the temporal mismatch of the prior inventory.

However, distinct spatiotemporal heterogeneities and structural discrepancies emerge between the two top-down constraints, particularly during the winter season characterized by high aerosol loadings. Although MEIC-2023 indicates an overall decrease from MIX-2010, the decadal change is spatially nonuniform (Fig. S7). In parts of southern Hebei, MEIC-2023 emissions in January exceed their MIX-2010 values, and the positive POMINO adjustments in some of these grid cells are therefore consistent in direction with an independently estimated local redistribution of emissions. This directional agreement does not, however, establish that the magnitude of the posterior enhancement is accurate. Positive POMINO increments over parts of Liaoning, northwestern Hebei, and Shaanxi are not supported to the same extent by MEIC-2023, while the positive S5P-OFFL adjustments over southern China are inconsistent with the decrease represented by the bottom-up inventory. During the summer season (July 2023), the differences between the two inversions become less pronounced, with both posterior fields dominated by downward adjustments over most of the domain, although localized product-dependent differences remain (Fig. 6g, h).

The localized emission adjustments in winter highlight the necessity of validating top-down constraints against independent bottom-up benchmarks. Therefore, a grid-by-grid statistical comparison against the MEIC-2023 inventory is executed to evaluate the performance of each inversion, in order to independently verify both the spatial structures and absolute regional budgets. Before assimilation, the temporal mismatch of the MIX-2010 prior exhibits a substantial regional budget bias, with a Normalized Mean Bias (NMB) of 75.3% in January and 75.7% in July, despite maintaining a strong spatial correlation ($R = 0.89$) (Fig. 7a, d). Post-assimilation metrics for January 2023 reveal a trade-off between regional budget calibration and spatial structure alignment. The S5P-OFFL-driven inversion effectively mitigates the absolute numerical overestimation, successfully lowering the regional NMB to 30.2%. However, this regional optimization coincides with a degradation in spatial representation, as its R drops from 0.89 to 0.67 (Fig. 7b). The POMINO-driven inversion reduces the NMB to 51.5%, an improvement of 23.8 percentage points over the prior, while retaining a higher spatial correlation of 0.80 (Fig. 7c). Thus, relative to MEIC-2023, S5P-OFFL provides the closer regional budget in January, whereas POMINO shows the closer grid-scale spatial correspondence. Nevertheless, its absolute regional emission budget remains systematically elevated, resulting in a larger residual bias (NMB = 51.5%) against the benchmark. During summer, this trade-off resolves. As shown in Fig. 7e and f, the POMINO-driven inversion demonstrates high precision, compressing the absolute regional budget bias to an NMB of 10.0% (compared to 28.7% for S5P-OFFL) while maintaining a comparable spatial correlation ($R = 0.73$ versus 0.76 for S5P-OFFL). These results demonstrate that the relative performance of the two inversions is season- and metric-dependent: agreement in the regional budget does not necessarily coincide with agreement in the grid-scale spatial distribution, and neither retrieval provides a uniformly superior constraint across both seasons.

The initial SCD residuals (ΔSCD) show broadly similar winter

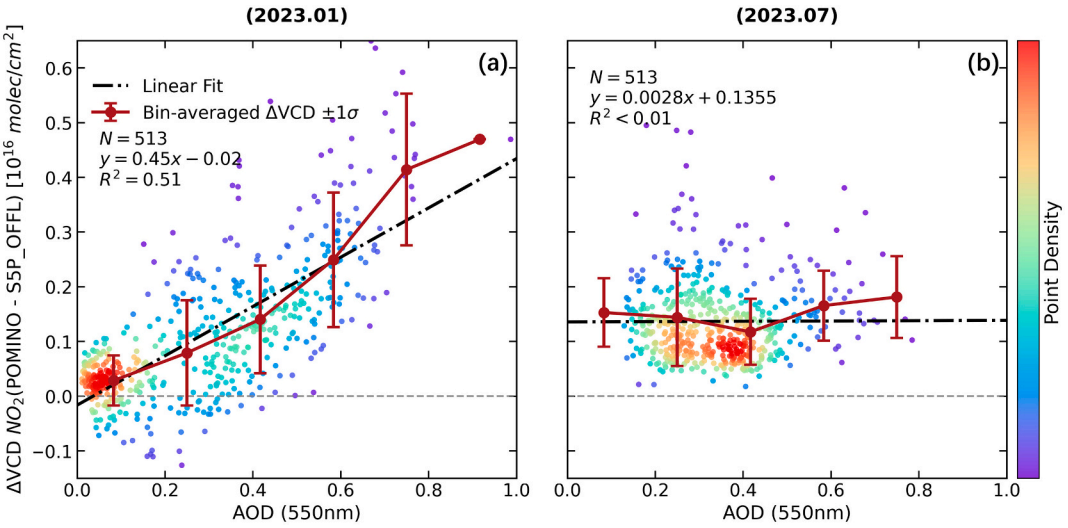


Fig. 4. Scatter-density plots illustrating the relationship between AOD and tropospheric NO_2 VCD differences ($\Delta VCD = VCD_{POMINO} - VCD_{S5P\text{-}OFFL}$) over the NCP for (a) January 2023 and (b) July 2023. The black dash-dotted lines represent the linear regression fits, with sample sizes (N), regression equations, and coefficients of determination (R) provided in each panel. The red solid lines and vertical error bars indicate the bin-averaged ΔVCD values and their corresponding standard deviations (±1σ), respectively. The colour scale indicates the data point density. (For interpretation of the references to colour in this figure legend, the reader is referred to the web version of this article.)

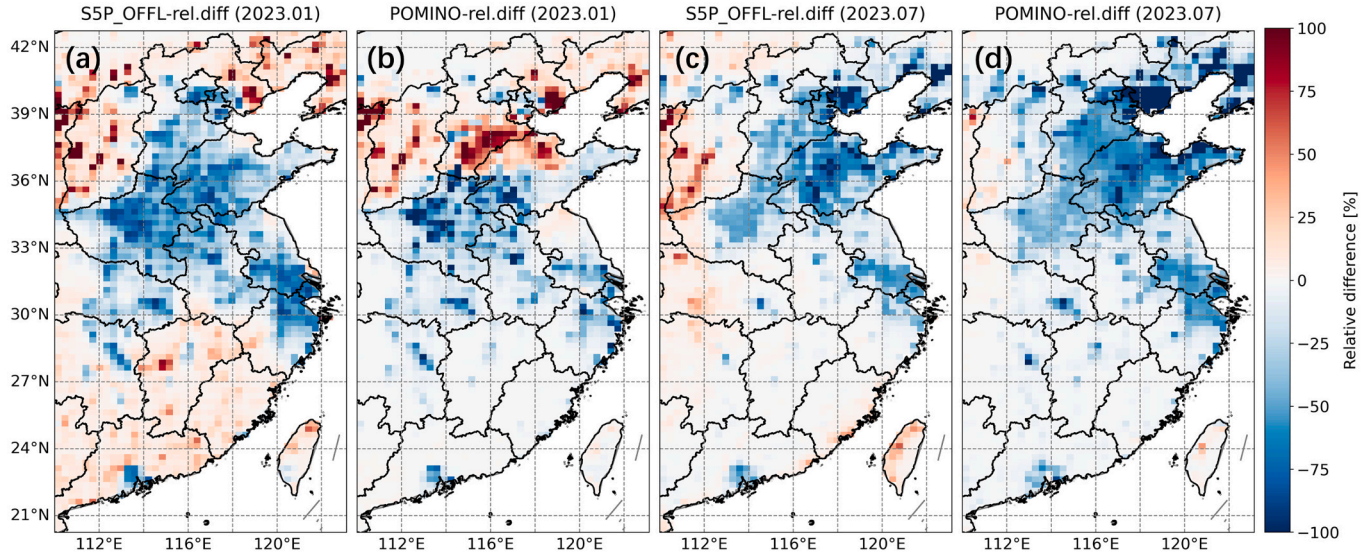


Fig. 5. Spatial distribution of relative difference (posterior versus prior) in anthropogenic NO_x emissions derived from assimilating S5P-OFFL NO_2 (a) and POMINO NO_2 (b) in January 2023. Panels (c) and (d) show the corresponding relative differences for July 2023.

patterns for the two products, with negative values over parts of western and northern China and positive values over central and eastern China (Fig. S8). The negative S5P-OFFL residuals over parts of southern China are also consistent with an initial tendency to increase emissions there. In July, POMINO residuals are predominantly positive across the domain, whereas positive S5P-OFFL residuals are concentrated over the NCP, Shandong, Jiangsu, and major cities, with weakly negative or near-zero values elsewhere. The emission adjustments derived from the S5P-OFFL inversion generally align with the SCD deviations between the a priori model and satellite observations, whereas the POMINO January inversion shows a localized positive adjustment in southern Hebei. Meanwhile, Fig. S8(a, c) shows that the differences between POMINO and S5P-OFFL in the January observed SCD are small, suggesting that the discrepancies between the two inversion results may stem more from differences in the observational operators and vertical sensitivities. POMINO's treatment of AMF differs from that of official products; this difference is particularly significant in the North China Plain during high-pollution winter months when NO_2 is concentrated near the ground, and may alter the sensitivity of local and downwind observations to emissions. Therefore, the positive adjustment in southern Hebei is more likely to reflect spatial redistribution within the inversion system and differences in observational sensitivity. It should be noted that emission optimization in the inversion is not directly determined by localized SCD differences, but rather depends on regional observational constraints that have been weighted by observational errors and propagated through chemical transport and associated sensitivities. The POMINO inversion uses γ value 7.5 times that used for S5P-OFFL, assigning greater relative weight to the prior term and thereby partly offsetting the stronger contribution of the observation term (Fig. S2).

The common-weight sensitivity experiment shows that the January POMINO posterior changes when the observation-error field and regularization parameter are replaced jointly. Applying the S5P-OFFL

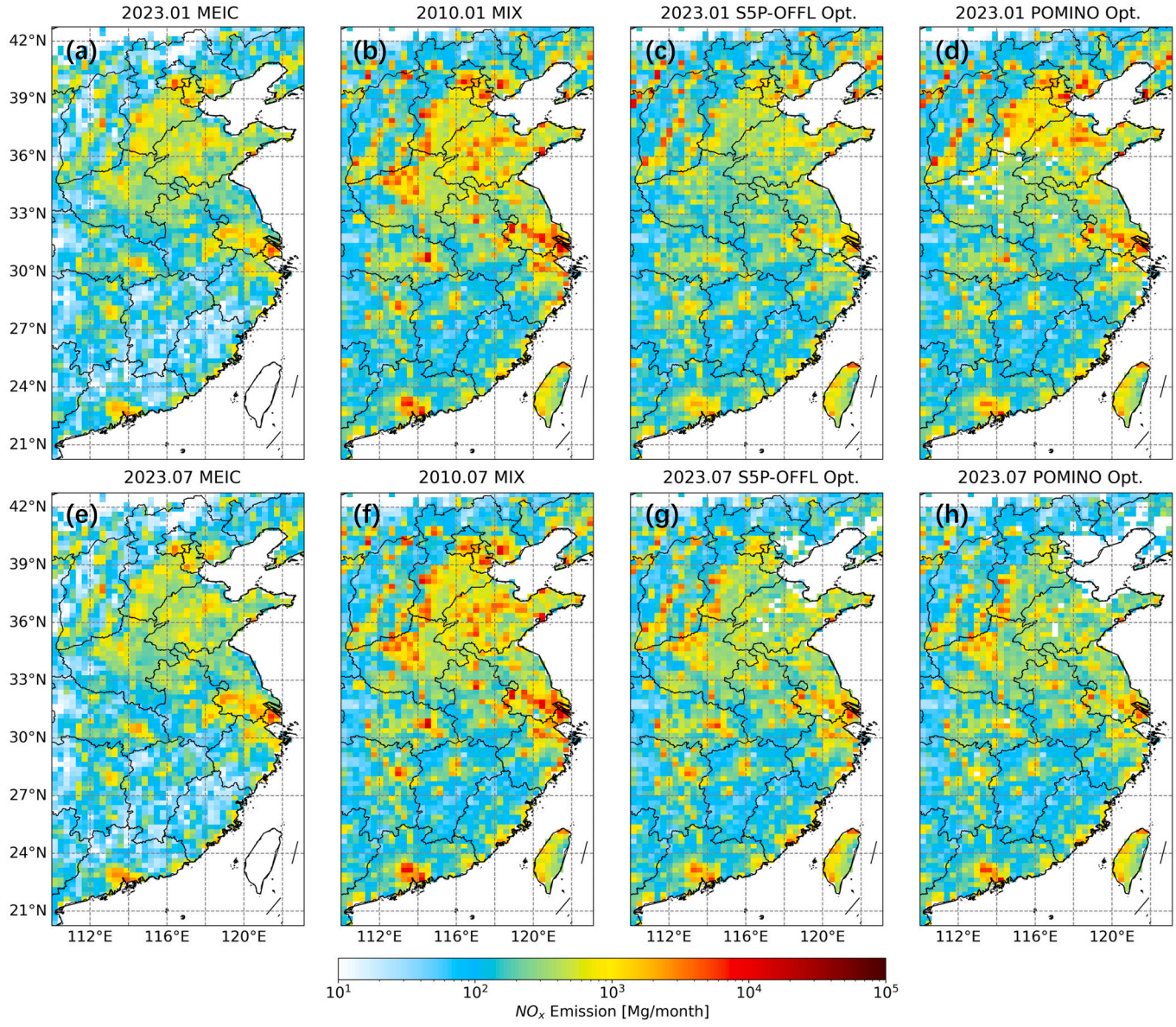


Fig. 6. Spatial distributions of surface NO_x emissions (Mg/month) in January (top row) and July (bottom row) 2023. Columns represent: (a, e) the independent bottom-up inventory MEIC v2.0 for 2023; (b, f) the prior inventory MIX 2010; (c, g) posterior emissions derived from S5P-OFFL NO_2 assimilation; and (d, h) posterior emissions derived from POMINO NO_2 assimilation.

observation errors and γ to POMINO attenuates the positive emission adjustments over the southern NCP and decreases the corresponding posterior surface and column NO_2 fields, whereas the July posterior changes less markedly. Because the observation-error field and γ were changed simultaneously, this experiment diagnoses sensitivity to the combined weighting configuration. The different aerosol treatments contribute to the contrasting winter signals retained by the two retrievals, whereas the magnitude of the resulting emission adjustments is also influenced by the combined observation-error and regularization configuration.

Differences between the posterior estimates and the MEIC-2023 benchmark are also influenced by the inherent structural limitations of the bottom-up inventory itself. The MEIC-2023 inventory relies on spatial proxy variables to downscale regional statistics to grid cells, a process that inevitably smooths local gradients. Furthermore, statistical data often fail to fully capture emissions from the residential sector, particularly the widespread use of dispersed coal for winter heating in rural and peri-urban areas (Xing et al., 2024). These dispersed small-scale emission sources are often underestimated in official energy statistics, although their contribution to total NO_x emissions is limited.

Overall, neither product provides a universally flawless constraint across all conditions. The S5P-OFFL product shows a more spatially consistent overall reduction in anthropogenic NO_x emissions relative to the MIX-2010 prior in both winter and summer, broadly consistent with the expected long-term emission decline in China, although its winter posterior exhibits reduced spatial correlation with MEIC-2023. In contrast, the POMINO inversion better preserves the spatial heterogeneity of winter emissions and captures localized weak increases over parts of the North China Plain that are also indicated by MEIC-2023, while tending to overestimate their absolute magnitude. In summer, POMINO yields a lower bias in the regional total emission estimate.

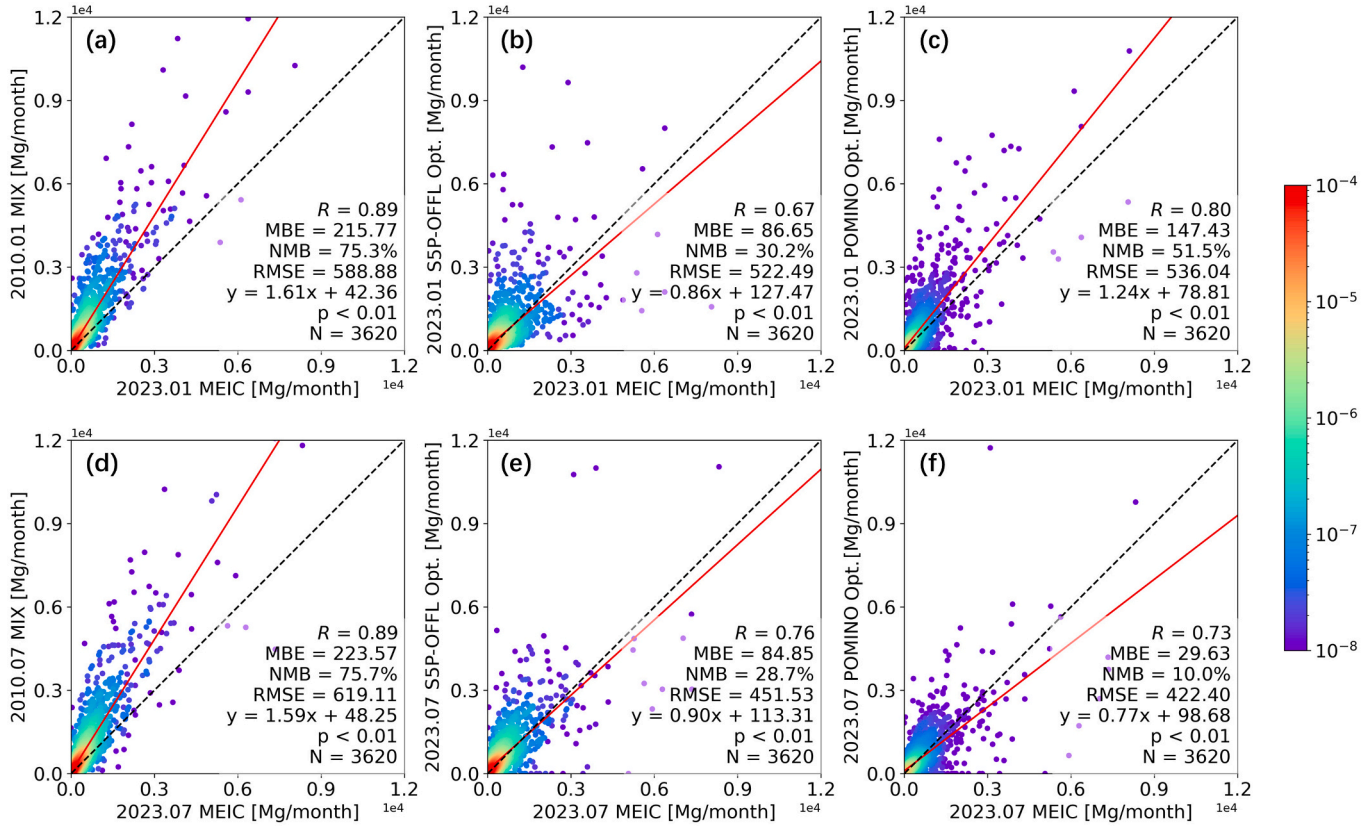


Fig. 7. Comparison of grid-scale monthly anthropogenic NO_x emissions (Mg/month) over China. The top row (a-c) represents January 2023, and the bottom row (d-f) represents July 2023. The x-axis in all panels denotes the benchmark emissions from the MEIC inventory for 2023. The y-axes represent: (a, d) emissions from the MIX inventory for 2010; (b, e) posterior emissions optimized using TROPOMI S5P-OFFL (official) NO_2 products; and (c, f) posterior emissions optimized using TROPOMI POMINO NO_2 products. The colour scale indicates the data density of grid cells. The solid red line represents the reduced major axis regression, while the dashed black line indicates the 1:1 line. (For interpretation of the references to colour in this figure legend, the reader is referred to the web version of this article.)

4. Evaluation of simulated NO_2 concentration driven by posterior emissions

4.1. Improvement of surface NO_2 concentration

Fig. 8 illustrates the spatial distribution of surface NO_2 concentrations over Eastern China in January and July 2023. Simulations driven by the MEIC-2023 benchmark inventory reproduce the observed regional gradients, though the grid-scale peak values are lower than the localized hotspots observed in situ, where winter concentrations frequently exceed 40 μg/m^3. This underestimation is typical of the volume-averaging effect inherent in model grid cells, which dilute sub-grid point-source peaks. However, the persistence of the low bias even in the MIX-2010 simulation, which is based on an older inventory with generally higher anthropogenic NO_x emissions than expected for 2023, suggests that spatial averaging alone may not fully explain the discrepancy. Uncertainties in the modeled lower-tropospheric NO_2 profile may also contribute to this underestimation, as GEOS-Chem may not fully capture the strong near-surface enhancement of urban NO_2 (Kharol et al., 2015; Lin et al., 2014). Compared with the MEIC-2023 and posterior simulations, the MIX-2010 simulation produces more extensive high-concentration plumes over the YRD, exceeding 45 μg/m^3 in some winter grid cells. In winter, however, the two posterior fields diverge significantly. The simulation constrained by S5P-OFFL shows lower surface NO2 concentrations of approximately 10–20 μg/m^3, whereas the POMINO-constrained simulation retains higher values of approximately 20–35 μg/m^3. The POMINO-constrained simulation is closer in magnitude to some observed high concentrations over both the YRD and parts of the NCP.

In summer, the posterior simulations constrained by S5P-OFFL (Fig. 8i) and POMINO (Fig. 8j) exhibit convergent spatial patterns. Both satellite constraints effectively mitigate the localized overestimations present in the MIX-2010 prior over the NCP and YRD, adjusting regional concentrations down to a baseline of 5–15 μg/m^3, which agrees with the MEIC-2023 driven fields (Fig. 8h). The better agreement in summer is likely associated with stronger boundary-layer mixing and more active photochemistry, which reduce near-surface NO_2 concentrations and spatial heterogeneity, thereby alleviating the representativeness mismatch between point observations and grid-averaged model fields.

To evaluate the statistical fidelity of the simulation results driven by different NO_2 inversion products, statistical metrics are shown in Table 1. for simulations driven by the MIX-2010 prior, MEIC-2023 reference benchmark, S5P-OFFL-assimilated posterior, and POMINO-assimilated posterior. The results respectively present the simulation results driven by the MIX-2010 prior, MEIC-2023 reference benchmark, S5P-OFFL-assimilated posterior, and POMINO-assimilated posterior.

The correlation coefficients across all scenarios generally fall within a moderate range (R ≈ 0.48–0.51) in January, reflecting that surface concentrations under winter conditions are primarily governed by large-scale meteorological forcing and primary emissions. However, the RMSE values remain substantial (17–21 μg/m^3), indicating persistent discrepancies between simulations and observations. While, the correlation coefficients are substantially lower ($R < 0.1$) in July across all scenarios, including the prior inventories. This suggests that active photochemical reactions and strong local convective processes during summer lead to more fragmented spatial distributions of surface NO_2 concentrations, complicating the ability of the modeling framework to capture spatial

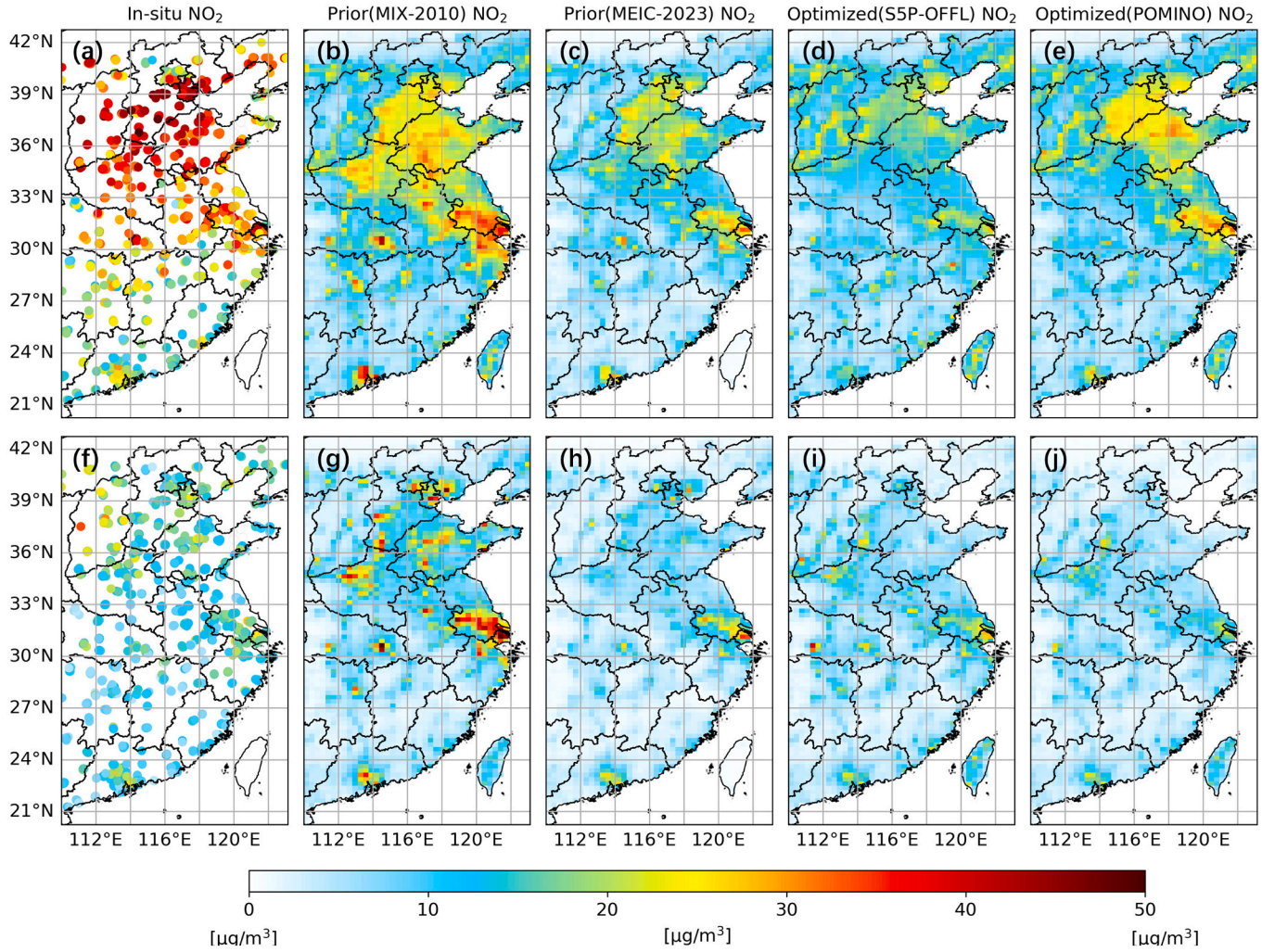


Fig. 8. Spatial comparisons of surface NO_2 concentrations over Eastern China for January (top row, a-e) and July (bottom row, f-j) 2023. Columns from left to right represent: (a, f) in-situ observations; (b, g) prior simulations driven by the MIX-2010 inventory; (c, h) reference simulations driven by the MEIC-2023 inventory; (d, i) posterior simulations assimilated with S5P-OFFL NO_2 product; and (e, j) posterior simulations assimilated with POMINO NO_2 product.

Table 1
Statistical metrics of surface NO_2 simulations over Eastern China. Values outside parentheses denote January, while values within parentheses denote July.

Scenario	R	σ (μg/m^3)	RMSE (μg/m^3)
Observation	1.00 (1.00)	9.56 (4.74)	/
Prior-MIX2010	0.49 (0.10)	8.44 (7.13)	17.21 (9.89)
Prior-MEIC2023	0.49 (0.10)	6.83 (3.93)	21.03 (10.44)
Optimized-S5P-OFFL	0.48 (0.07)	5.29 (3.33)	20.37 (9.99)
Optimized-POMINO	0.51 (0.03)	6.82 (4.26)	19.21 (10.49)

variability. Even when the MEIC-2023 inventory is used as prior input, accurately reproducing observations remains challenging.

The winter statistical metrics demonstrate that the observed in-situ standard deviation is 9.56 μg/m^3. After assimilating the S5P-OFFL product, the simulated σ decreases to 5.29 μg/m^3, while the POMINO-constrained posterior yields a higher σ of 6.82 μg/m^3, closer to the observed variability. The posterior correlation coefficients are 0.48 for S5P-OFFL and 0.51 for POMINO, and the corresponding RMSE values are 20.37 μg/m^3 and 19.21 μg/m^3, respectively. These differences indicate that the two retrieval products lead to modestly divergent spatial variability in the winter posterior simulations, with the POMINO-driven inversion retaining a σ closer to the observed level.

In summer, the statistical characteristics are dominated by the correction of structural biases in the prior inventory. The MIX-2010 prior exhibits a σ of 7.13 μg/m^3 and a low correlation coefficient of 0.10, both confirming that the outdated prior inventory overestimates local emission intensities and introduces excessive spatial variability. The observed σ is 4.74 μg/m^3. After assimilation, S5P-OFFL and POMINO reduce σ to comparable levels of 3.33 μg/m^3 and 4.26 μg/m^3, respectively, while producing similarly low R of 0.07 and 0.03. The close similarity between the two posterior metrics indicates that, under the low-aerosol summer conditions over eastern China, the dominant error source is the bias inherent in the prior inventory rather than differences in the satellite retrieval algorithm.

It should be noted that the chemiluminescence analyzers with molybdenum converters employed by the CNEMC network are subject to interference from other oxidized nitrogen species (NO_z, including peroxyacetyl nitrate, HNO_3, and organic nitrates), which can lead to a systematic overestimation of NO_2 concentrations, particularly during winter when NO_z levels are elevated and NO_x lifetimes are longer (Liu et al., 2018; Zhang et al., 2023). This measurement bias has distinct implications for the seasonal results reported above. In winter, the observed NO_2 concentrations are expected to carry a larger positive bias from NO_z interference; consequently, the apparent model underestimation and the magnitude of the reported RMSE are partly attributable to this measurement artifact rather than to model errors alone. In summer, stronger photochemical activity and shorter NO_x lifetimes

suppress the accumulation of NO_z, making the CNEMC measurements a more reliable benchmark for evaluating model performance. Liu et al. (2018)estimated that correcting this interference reduced regional mean hourly NO_2 concentrations over eastern China by approximately 2 to 30 μg/m^3 during autumn and early winter, although GEOS-Chem still underestimated the corrected observations by about 17 μg/m^3 on average. These findings suggest that measurement interference may contribute to the winter discrepancy between simulations and observations in Fig. 8; however, its contribution in our study remains unquantified and cannot be assumed to explain all or most of the discrepancy. This uncertainty should be considered when interpreting the statistics in Table 1, while differences among the simulated fields remain informative.

Despite improvements in some statistical metrics, differences between simulated and observed surface NO_2 concentrations may reflect the combined effects of spatial averaging within model grids, uncertainties in the modeled vertical profiles, and interference in the measurements. To separate the magnitude bias arising from scale mismatch and to evaluate the capability of retrieval algorithms in reconstructing the spatial patterns of NO_2, we employed the global Moran's I and Local Indicators of Spatial Association (LISA) analyses (Anselin, 1995; Moran, 1950). This approach allows for an assessment of how different products capture the spatial clustering characteristics of pollution. The statistical indicators are summarized in Table 2. A detailed description of the relevant formulas can be found in Text S3 of the supplementary file.

Seasonal variations in atmospheric lifetimes and vertical mixing scales strongly modulate the baseline spatial autocorrelation of surface NO_2. During the warmer months, enhanced convective transport and accelerated photochemical sinks fragment the regional pollution field, as indicated by the suppressed observational global Moran's I of 0.45. Both POMINO (0.43) and S5P-OFFL (0.44) posterior simulations closely capture this fragmented configuration. The comparable LISA cluster consistency rates (39.36% for S5P-OFFL and 35.15% for POMINO) along with minimal outlier misidentification rates demonstrate that under low aerosol loadings, the data assimilation framework exhibits low sensitivity to the underlying satellite retrieval formulation, with both products replicating the baseline spatial structure.

During the transition to wintertime, stagnant regional meteorology and prolonged NO_2 chemical lifetimes amplify the spatial aggregation of pollution hotspots, elevating the observed global Moran's I to 0.65. Within this high-aerosol background, the spatial reconstruction capacities of the two retrieval algorithms diverge significantly. The S5P-OFFL-driven posterior yields a degraded global Moran's I of 0.60 and a LISA cluster consistency rate restricted to 56.58%. As illustrated in the LISA difference (Fig. S4), the S5P-OFFL inversion exhibits a higher proportion of misidentified outliers (9.43%) in the core region of the NCP. This observation reinforces our previous findings: the signal smoothing effect induced by implicit aerosol correction not only suppresses peak concentrations but also spatially blurs the gradients of pollution plumes, leading to a harmonized simulation field that underrepresents the steep spatial structures observed in situ.

The POMINO-driven inversion, by comparison, yields an enhanced winter global Moran's I of 0.76. This elevated correlation is partially a structural consequence of the model's grid volume-averaging effect, which inherently smooths sub-grid heterogeneity and enhances spatial continuity relative to discrete point observations. However, the sharp contrast with the S5P-OFFL performance indicates that retrieval-induced spatial noise can easily override this model-driven continuity. By utilizing explicit aerosol-corrected satellite signals, the POMINO framework preserves local pollution gradients, securing a winter LISA consistency rate of 58.81% and restricting the outlier misidentification rate to 5.71%.

The structural configuration of high-value emission clusters is further resolved via the Getis-Ord statistic (Getis and Ord, 1992). As shown in Table 3, the observed global *Z*-score of 15.47 for January, the S5P-OFFL simulation produces value of 22.21, confirming that its implicit retrieval algorithm merges localized plumes into artificial, continuous high-concentration blocks. Conversely, the POMINO-driven simulation yields a Z-score of 17.35, which aligns more closely with the observational baseline. Explicitly resolving aerosol optical properties under heavy winter haze preserves localized sub-grid gradients, thereby restraining the unphysical expansion of high-value clusters inherent to the modeling framework.

4.2. Verification of tropospheric NO_2 column densities

While ground-based measurements provide high-frequency near-surface constraints, their spatial representativeness is limited by station density. Validating against satellite-retrieved column densities provides a broader, spatially continuous perspective to evaluate the regional-scale NO_2 distribution and overall tropospheric abundance. We harmonized the vertical profiles of all satellite products (OMI, S5P-OFFL, and POMINO) by replacing them with coincident GEOS-Chem model profiles prior to comparison, thereby eliminating systematic biases arising from inconsistent prior profile assumptions. Following data assimilation, the simulated monthly average NO_2 VCD were compared to evaluate the combined effects of product-specific retrieval sensitivities, observation weighting, and regularization on the posterior simulations.

Fig. 9 illustrates the spatial distribution comparison and statistical validation under winter pollution conditions in January 2023. While the NO_2 VCD simulation driven by the prior emission inventory (Fig. 9f) captures the fundamental distribution pattern of NO_2 pollution across eastern China, its overall intensity is markedly higher than all satellite observations (Fig. 9a-c). The S5P-OFFL-based assimilation attempts to rectify this but results in a substantial downward adjustment. In heavily polluted core areas such as the NCP, its simulated NO_2 column densities (Fig. 9d) are lower than satellite observations. The corresponding SCD diagnostics show that assimilation reduces the initially positive S5P-OFFL residuals over central and eastern China, but produces extensive negative residuals over the NCP and YRD (Fig. S10). The high values along the northern edge of Fig. 9a coincide with a high occurrence of snow-covered observations (Fig. S11), suggesting that snow-related retrieval sensitivity may contribute to this feature. However, the snow occurrence is much lower farther south, indicating that snow cannot explain the entire enhancement. Thus, although the total cost decreases substantially, the S5P-OFFL inversion does not fully reproduce the observed January columns and appears to produce an overly strong downward adjustment in some regions. By contrast, the POMINO-driven

Table 2
Summary of spatial autocorrelation statistics for surface NO_2 concentrations in January and July 2023, including Global Moran's I and the percentage of consistency in Local Indicators of Spatial Association (LISA) cluster types between simulations and in-situ observations. Values outside parentheses denote January, while values within parentheses denote July. All Global Moran's I values are statistically significant with $p < 0.001$.

	Observation	Simu-S5P-OFFL	Simu-POMINO
Moran's global I	0.65 (0.45)	0.60 (0.44)	0.76 (0.43)
Consistent	/	56.58% (39.36%)	58.81% (35.15%)
Hotspot Missing	/	16.63% (23.02%)	17.37% (24.01%)
Coldspot Missing	/	9.43% (16.58%)	10.42% (17.33%)
Outlier	/	9.43% (13.37%)	5.71% (15.59%)
Inconsistent	/	7.94% (7.67%)	7.69% (7.92%)

Table 3
Z-score of the global Getis-Ord G (high-value aggregation), with $p < 0.05$.

	Observation	Simu-S5P-OFFL	Simu-POMINO
January	15.47	22.21	17.35
July	12.72	14.58	14.78

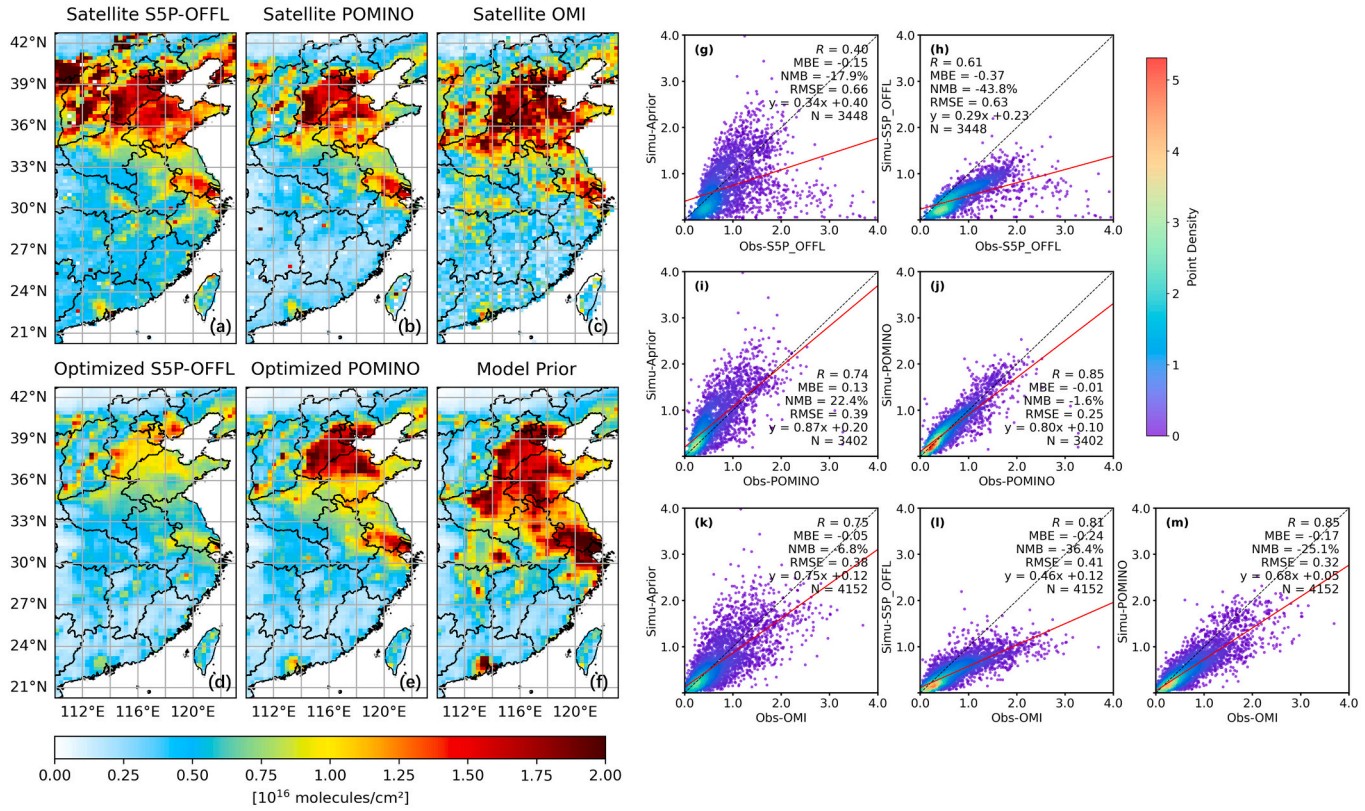


Fig. 9. Spatial comparison and scatter validation of tropospheric NO_2 vertical column densities over Eastern China (January 2023). The left panels display spatial distributions of: (a) TROPOMI-S5P-OFFL NO_2 VCD observations, (b) TROPOMI-POMINO NO_2 VCD observations, (c) independent NO_2 VCD observations from OMI, (d) the posterior simulation constrained by the TROPOMI-S5P-OFFL product, (e) the posterior simulation constrained by the TROPOMI-POMINO product, and (f) the GEOS-Chem simulation using prior emissions. The right panels present scatter comparisons between simulated and observed NO_2 VCD: (g) a-priori simulation versus TROPOMI-S5P-OFFL, (h) S5P-OFFL-based posterior simulation versus TROPOMI-S5P-OFFL, (i) a-priori simulation versus TROPOMI-POMINO, (j) POMINO-based posterior simulation versus TROPOMI-POMINO, (k) a-priori simulation versus OMI, (l) S5P-OFFL-based posterior simulation versus OMI, and (m) POMINO-based posterior simulation versus OMI. The solid red lines represent the linear regression fits, and the dashed black lines indicate the 1:1 reference lines. (For interpretation of the references to colour in this figure legend, the reader is referred to the web version of this article.)

posterior (Fig. 9e) maintains the structural integrity of the pollution hotspots. It achieves higher spatial consistency with OMI observations (Fig. 9m), improving the correlation coefficient to 0.85 with a NMB of −25.1%. Under the original inversion configurations, the POMINO-driven posterior also retains higher NO_2 columns over several megacities and densely populated urban clusters, including Guangzhou. This pattern is consistent with enhanced retrieval sensitivity under aerosol-polluted conditions and contributes to closer agreement with the independent OMI observations. However, it should be interpreted as improved observational consistency under the present configuration rather than definitive evidence that either the POMINO retrieval or the resulting posterior emissions are universally more accurate, because the two inversions also differ in observation-error specification and regularization and remain affected by model structural uncertainties. In prominent urban centers such as Guangzhou, the POMINO-driven posterior achieves a more realistic representation of localized NO_2 hotspots. By explicitly accounting for aerosol optical properties, POMINO recovers the previously masked NO_2 signals, yielding higher column densities in haze-polluted regions. This reduces the artificial difference between the prior simulation and observations, thereby preventing the assimilation system from making an excessive downward adjustment to the prior emissions, ensuring that the spatial gradient between urban and rural areas remains physically consistent.

In the July 2023 summer scenario (Fig. 10), the prior-inventory-driven column concentration simulations showed a clear overestimation trend in the YRD and NCP regions (Fig. 10f). The statistical performance in July indicates that both inversion schemes corrected the overestimation resulting from the initial inventory assumptions (Fig. 10g-m). Specifically, the previous simulation exhibited a steep slope of 1.72 and a large positive bias relative to OMI (NMB = 30.6%) (Fig. 10k). Inversions constrained by the S5P-OFFL and POMINO NO_2 products both successfully eliminated this bias, bringing the regression slope closer to 1 and significantly reducing the NMB. Notably, the S5P-OFFL-driven posterior simulation effectively reduced the overall emission intensity, with a slope of 0.90 and minimal bias (NMB = −2.8%). The POMINO-driven posterior simulation also demonstrated an available correction effect, with a slope of 0.71 and a moderate underestimation (NMB = −14.3%). The similar correlation coefficients in summer (R = 0.75–0.77) suggest that under cleaner atmospheric conditions, the advantage of explicit aerosol correction becomes less dominant compared to winter. The shorter atmospheric lifetime of NO_2 and more active convective transport mean that both products impose similar constraints on the assimilation of anthropogenic emissions during the summer.

It should be noted that the remaining discrepancies between the posterior simulations and satellite VCDs do not necessarily indicate a lack of convergence of the inversion, nor can they be attributed solely to errors in the inferred NO_x emissions. The inversion is optimized in error-weighted tropospheric SCD space and is simultaneously constrained by the prior emissions; therefore, its objective is not to reproduce the monthly mean VCD field exactly at each grid cell. In addition, the two inversions adopt different observation-error specifications. The observation errors assigned to POMINO are generally smaller than those of S5P-OFFL, resulting in a stronger observational constraint, while the

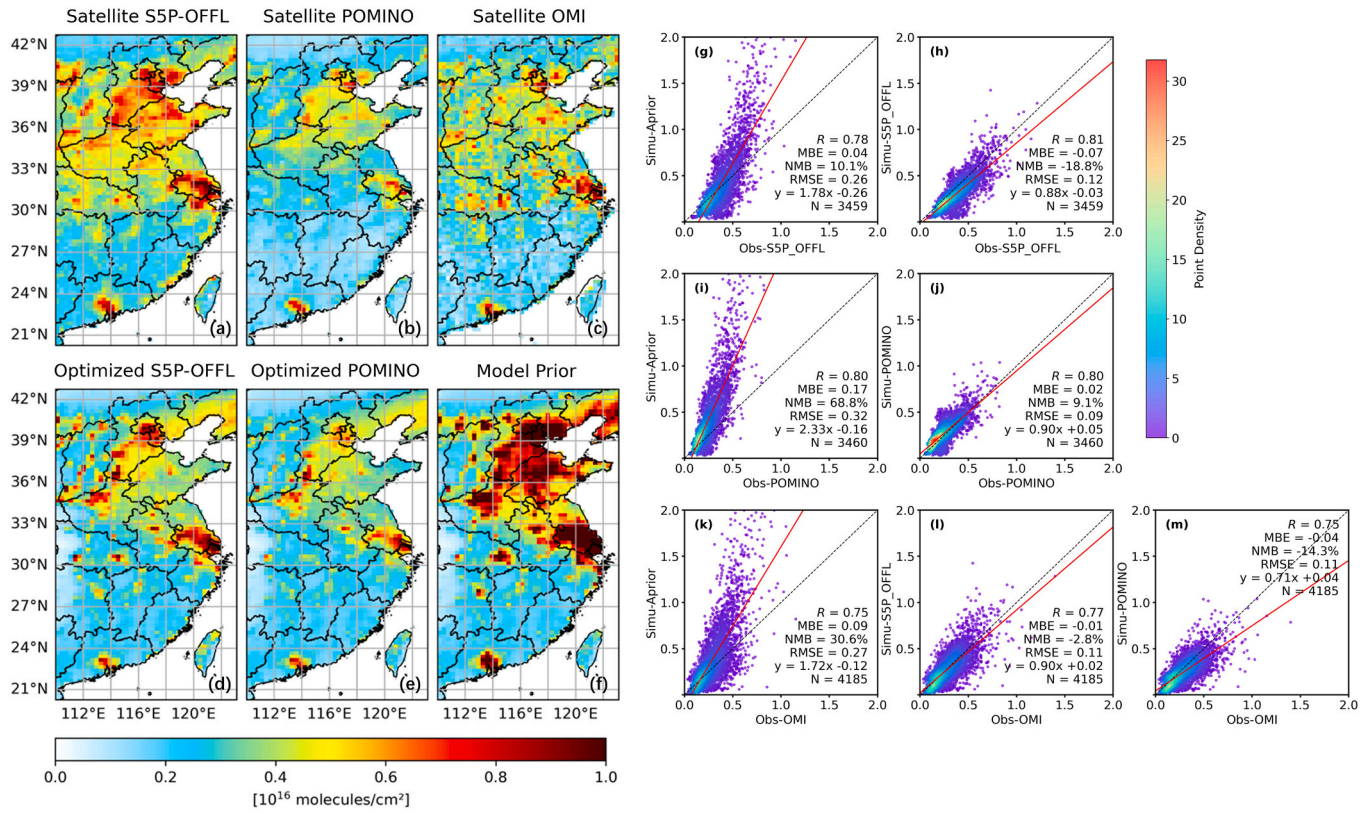


Fig. 10. Similar to Fig. 9, but for July 2023.

larger regularization parameter used for POMINO partly compensates for this stronger observational weighting.

Another source of uncertainty arises from the chemical environment represented by the forward model. The inversion optimizes anthropogenic NO_x emissions, whereas other chemical conditions controlling the NO_x lifetime and NO_2 partitioning remain prescribed by the forward-model configuration (Shah et al., 2020). Because the anthropogenic emission framework used here is largely based on the older HTAP/MIX inventory, co-emitted precursors other than NO_x may not fully represent the atmospheric chemical environment of 2023. Changes in VOC and CO emissions, for example, can modify OH and peroxy-radical abundances and thereby influence NO_x oxidation and NO-NO_2 partitioning (Atkinson, 2000), whereas changes in SO_2, NH_3, and aerosol composition can affect aerosol surface area and heterogeneous loss processes such as N_2O_5 uptake (Bertram and Thornton, 2009), which are particularly important during winter. Consequently, part of the model–observation mismatch may arise from a temporally inconsistent chemical environment that is not directly adjusted by the inversion.

Although common GEOS-Chem NO_2 vertical profiles were applied to reduce the influence of inconsistent a-priori profile assumptions among the satellite products, the simulated vertical distribution of NO_2 remains sensitive to boundary-layer mixing, the representation of the wintertime stable boundary layer, and chemical processes. These uncertainties can affect both near-surface NO_2 and the column response represented by the observation operator and may therefore be partially absorbed into the optimized emissions. Accordingly, the closer agreement of the POMINO-constrained posterior with OMI during winter should be interpreted as improved observational consistency under the present inversion configuration and polluted conditions, rather than as direct evidence that either the retrieval itself or the resulting posterior emissions are universally more accurate. Future work combining updated co-emitted precursor emissions, more recent chemical mechanisms, targeted sensitivity experiments on chemical and boundary-layer processes, and high-resolution NO_2 vertical-profile observations would help further separate retrieval, model, and emission uncertainties.

5. Case studies under typical polluted and clean scenarios

To elucidate the underlying physical mechanisms driving the differences between S5P-OFFL and POMINO constraints and to validate the robustness of the adjoint inversion system, we conducted a detailed comparative analysis of two distinct scenarios. January 3, 2023, representing a severe haze case, and January 29, 2023, representing a clean background scenario are selected.

5.1. Pollution scenarios

On January 3, 2023, the NCP is dominated by a stagnant synoptic weather pattern, characterized by a weak pressure gradient and stable boundary layer conditions. As illustrated in Fig. 11f, the 850 hPa winds field indicates weak east-southeast wind prevailing over the region, facilitating the accumulation of pollutants. The AOD exceeded 1.0 across Hebei, Shandong, and Henan provinces, with core areas surpassing 1.5, indicating a severe regional haze event. Coincident surface monitoring data confirmed this assessment, with the AQI reaching heavily polluted levels (AQI $>$ 200) at multiple stations across the region (Fig. 11). This scenario presents a critical challenge for satellite NO_2 retrievals and provides an ideal scenario to evaluate the performance of satellite products under complex atmospheric environments.

While the GEOS-Chem model prior NO_2 VCD (Fig. 11k) captures the general spatial outline of the NCP pollution belt, it significantly underestimates the peak intensities. After applying consistent model NO_2 vertical profiles, both S5P-OFFL (Fig. 11c) and POMINO (Fig. 11d) satellite observations exhibit highly comparable spatial distributions and numerical magnitudes, successfully detecting elevated NO_2 columns over the peak AOD regions. Furthermore, the independent OMI observations (Fig. 11e) suffer from severe data loss over the core polluted area due to the thick aerosol layer, underscoring the necessity of high-

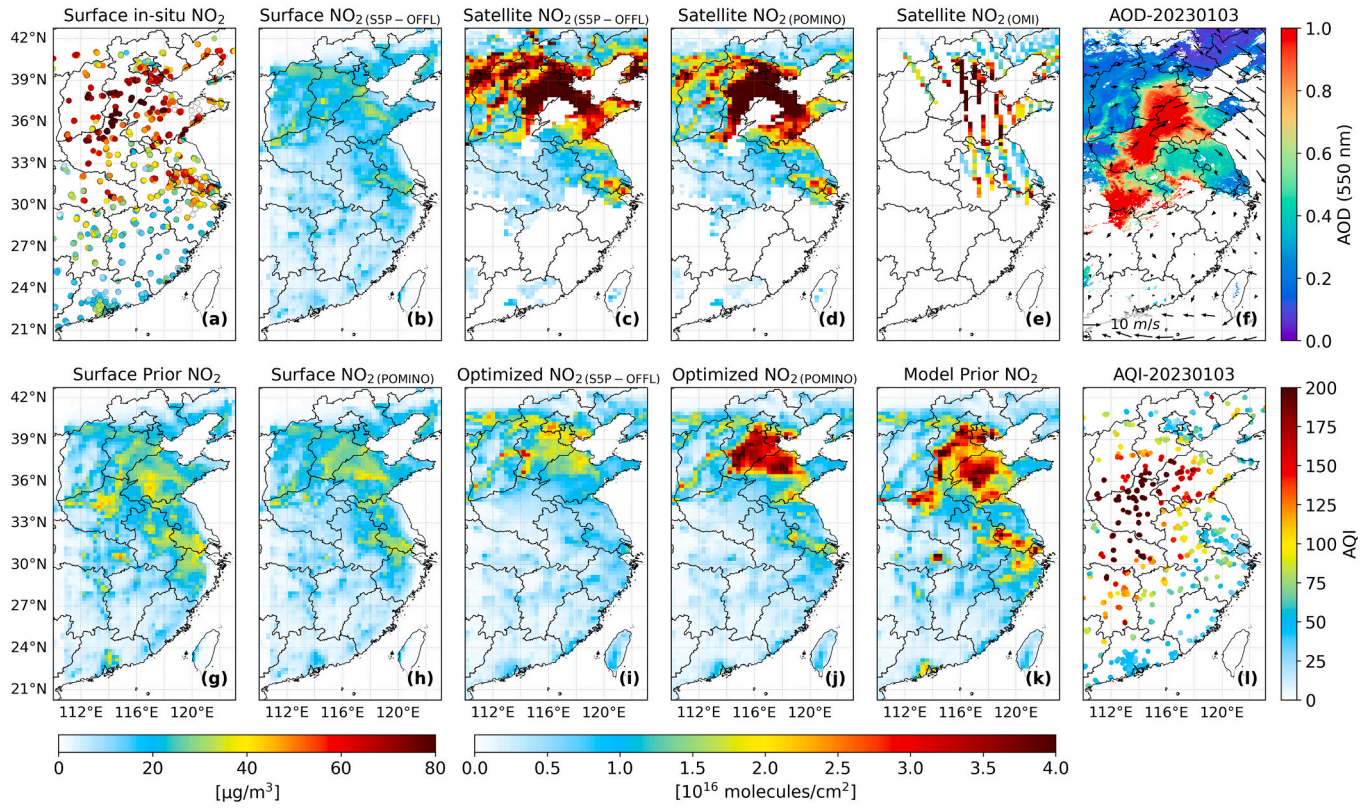


Fig. 11. Case study of a severe haze scenario on January 3, 2023. (a) Observed surface NO_2 concentrations from the in-situ network. GEOS-Chem simulated surface NO_2 concentrations using (g) prior emissions, (b) S5P-OFFL-constrained posterior emissions, and (h) POMINO-constrained posterior emissions. Satellite-observed tropospheric NO_2 VCD from (c) TROPOMI-S5P-OFFL, (d) TROPOMI-POMINO, and (e) OMI. GEOS-Chem simulated tropospheric NO_2 VCD based on (k) prior emissions (Forward), (i) posterior emissions constrained by S5P-OFFL, and (j) posterior emissions constrained by POMINO. (f) AOD at 550 nm overlaid with 850 hPa wind vectors. (l) Surface AQI distribution shows widespread heavy pollution.

resolution TROPOMI data for winter haze events. Despite the comparable magnitude of the observational inputs, their impacts within the assimilation system diverge significantly. The optimized NO_2 VCD driven by the S5P-OFFL product (Fig. 11i) displays a suppressed spatial field over the NCP, failing to reproduce the extreme column densities observed from space. Consequently, the S5P-OFFL-driven posterior ground-level NO_2 concentrations (Fig. 11b), while slightly higher than the prior simulations (Fig. 11g), still underrepresent the extreme concentration peaks observed by surface stations. Conversely, the POMINO-driven optimized VCD (Fig. 11j) successfully reconstructs the intense spatial core of the pollution episode. Correspondingly, the posterior ground-level NO_2 simulated by the POMINO-constrained model (Fig. 11h) yields a spatial distribution that much more closely matches the high-value in the surface observation over the NCP.

Quantification of data assimilation efficiency during this pollution episode is evaluated via the percentage reduction in RMSE for both near-surface concentrations and tropospheric VCD relative to the prior simulation (Fig. S5). To evaluate the statistical significance of the discrepancies between the two inversions across the spatial domain, a grid-cell-by-grid-cell Mann-Whitney *U* test was applied at the 95% confidence level, with non-significant differences masked in gray. At the surface level, the difference in RMSE reduction at individual monitoring stations is statistically indistinguishable from zero across the majority of locations. However, a pronounced spatial difference occurs in the tropospheric VCD error reductions (Fig. S5f). The difference map exhibits extensive negative values, ranging from −20% to −40%, across the central, southern, and eastern-coastal sectors of the domain. Given that the difference is defined as S5P-OFFL minus POMINO, these negative value demonstrate that the POMINO-driven posterior achieves a larger percentage reduction in column errors than the S5P-OFFL configuration over these regions. Conversely, positive values are confined to localized northern sections of the NCP, where the S5P-OFFL constraint demonstrates a larger error reduction. Because the two inversions use different observation-error fields and regularization parameters, this contrast should be interpreted as the combined effect of product-specific retrieval sensitivities and inversion weighting rather than as the effect of explicit aerosol treatment alone. Nevertheless, the spatial pattern is consistent with the possibility that the POMINO observation operator retains additional NO_2 information under high-AOD conditions, a contribution that should be evaluated under harmonized uncertainty settings.

5.2. *Clean air scenarios*

Evaluation of a clean-air background scenario on January 29, 2023, establishes whether the discrepancies observed under heavy pollution stem from aerosol parameterization schemes or inherent algorithmic biases. On this day, robust northerly wind vectors established favorable advection and dispersion conditions across Eastern China (Fig. 12). The regional mean AOD fell below 0.2 across the majority of the domain, maintaining low near-surface concentrations and baseline background conditions across major urban centers.

Under this clean background, the S5P-OFFL and POMINO constraints demonstrated high algorithmic convergence. The tropospheric NO_2 VCD derived from both products exhibited similar spatial distribution patterns and magnitudes, lacking the substantial spatial discontinuities observed during the haze pollution. Physically, in the absence of a strong scattering aerosol layer, the implicit correction scheme (S5P-OFFL) and the explicit aerosol correction scheme (POMINO) yield comparable AMF calculations. With negligible aerosol attenuation or brightening effects,

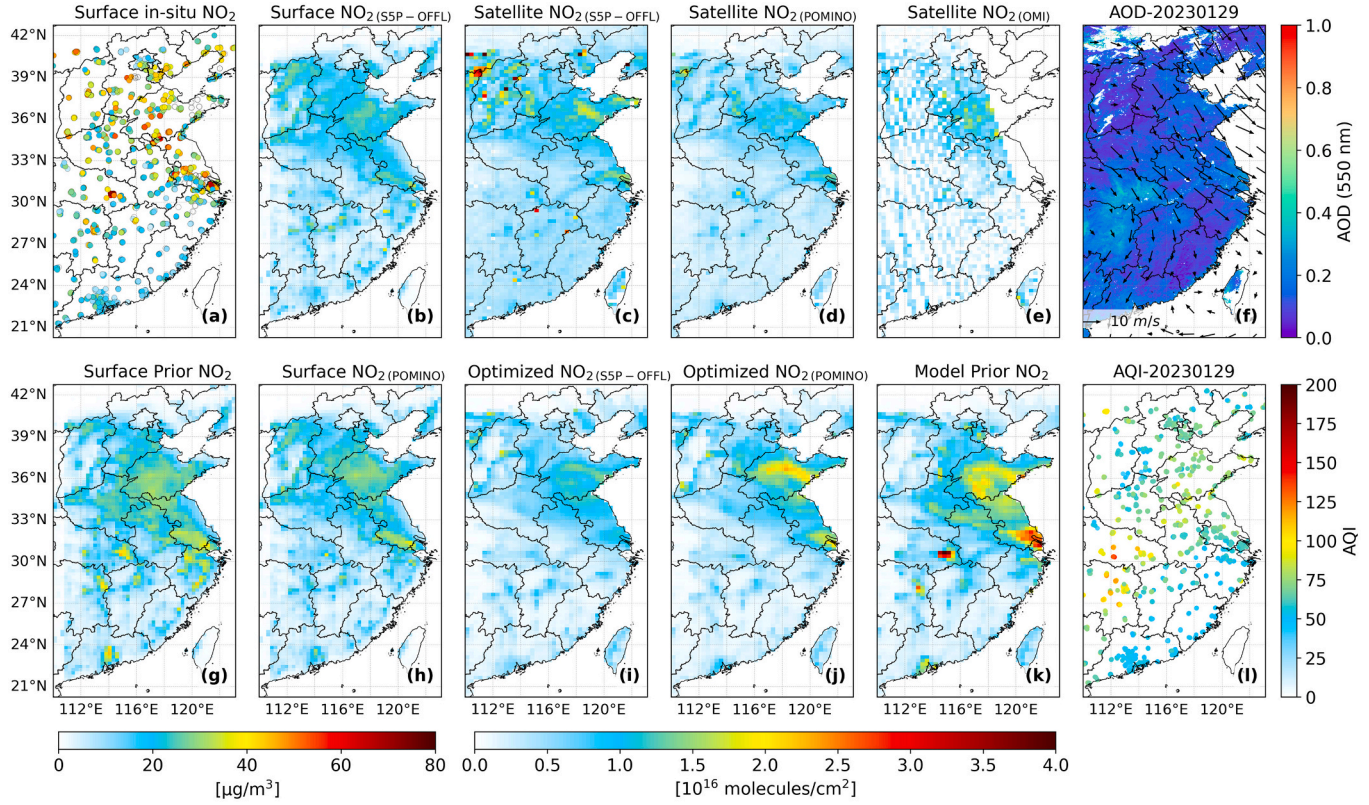


Fig. 12. Case study of a clean air scenario on January 29, 2023. The panel layout and variable descriptions are identical to Fig. 11, but represent a typical clean episode. Panel (l) presents the corresponding surface AQI distribution, illustrating overall clean air conditions across the region.

both algorithms capture near-surface NO_2 signals comparably.

The assimilation system shifts its primary focus from mitigating observational biases to optimizing inherent errors within the prior emission inventory. Because both products provide similar observational constraints under these conditions, the calculated assimilation gradients exhibit similar directions and magnitudes. Consequently, the posterior emission fields and their corresponding near-surface NO_2 simulations for both S5P-OFFL and POMINO exhibit highly similar spatial characteristics. Further quantitative evaluation of the RMSE reduction (Fig. S6) corroborates this broad algorithmic convergence across the domain. However, the VCD spatial difference map (Fig. S6f) highlights a cluster of negative values over South China, indicating that the POMINO-driven posterior achieves a marginally greater column error reduction in this specific region even under clean atmospheric conditions.

The difference between the polluted and clean cases is consistent with a greater influence of aerosol treatment under high aerosol loading, while both products provide similar constraints under clean conditions. Because other retrieval inputs and inversion-weighting settings also differ between the two configurations, this case comparison supports an aerosol-related contribution but does not uniquely isolate it or exclude additional retrieval and model uncertainties.

6. Conclusions

This study quantified how the choice of TROPOMI NO_2 retrieval product affects top-down anthropogenic NO_x emission estimates over eastern China. S5P-OFFL and POMINO observations were assimilated separately using the GEOS-Chem adjoint model for January and July 2023. The posterior emissions and NO_2 simulations were evaluated against the MEIC-2023 inventory, surface observations from 1282 monitoring stations, and independent OMI NO_2 columns. Three main conclusions are drawn.

(1) The two retrieval products produced season- and metric-dependent emission estimates. In January, the S5P-OFFL inversion reduced the regional emission bias relative to MEIC-2023 to 30.2%, compared with 51.5% for POMINO. POMINO preserved the grid-scale spatial pattern more effectively, with a correlation coefficient of 0.80 compared with 0.67 for S5P-OFFL. In July, both inversions corrected the overestimation in the MIX-2010 prior. POMINO achieved a lower regional bias than S5P-OFFL (10.0% versus 28.7%), while their spatial correlations were similar (0.73 versus 0.76). Regional emission budgets and grid-scale spatial patterns therefore provide complementary measures of inversion performance.

(2) POMINO provided stronger constraints on the spatial structure of winter NO_2 pollution under high aerosol loading. Compared with the S5P-OFFL posterior, the POMINO posterior reduced the surface NO_2 RMSE from 20.37 to 19.21 μg/m^3 and increased the correlation with surface observations from 0.48 to 0.51. POMINO also reproduced the observed spatial clustering more closely, with a global Moran's I of 0.76 and a LISA cluster consistency rate of 58.81%, compared with 0.60 and 56.58% for S5P-OFFL. Against independent OMI observations, the POMINO posterior achieved $R = 0.85$ and NMB $= -25.1\%$, whereas the S5P-OFFL posterior yielded $R = 0.81$ and NMB $= -36.4\%$. During the severe haze episode, POMINO produced larger reductions in column RMSE across extensive central, southern, and eastern coastal regions. The two posterior simulations became more similar in summer and during the clean-air episode.

(3) The explicit aerosol treatment in POMINO contributed to the stronger NO_2 constraint under high-AOD conditions. The magnitude of the posterior differences was further controlled by the observation-error fields, regularization parameters, and the model representation of winter NO_x loss. Applying the S5P-OFFL observation errors and regularization parameter to POMINO

reduced the positive January emission adjustments, directly demonstrating the influence of inversion weighting. Uncertainties in heterogeneous N_2O_5 uptake, lower-tropospheric NO_2 profiles, and the chemical environment represented by the prior emissions also affected the inferred emission magnitude.

Overall, POMINO better preserved winter pollution hotspots and regional NO_2 gradients, while the relative performance of POMINO and S5P-OFFL varied with season and evaluation metric. The results establish aerosol treatment as an important component of winter NO_x emission inversion and show that its influence must be evaluated together with observation weighting, regularization, and atmospheric model processes.

CRediT authorship contribution statement

Wenhui Dong: Writing – original draft, Visualization, Validation, Methodology, Investigation, Formal analysis, Data curation, Conceptualization. **Yi Wang:** Writing – review & editing, Validation, Supervision, Software, Resources, Methodology, Conceptualization, Funding acquisition. **Yanyu Wang:** Supervision, Funding acquisition, Methodology. **Jiajun Xiong:** Writing – review & editing, Software, Methodology, Data curation. **Jintai Lin:** Writing – review & editing, Methodology, Data curation. **Mengying Wang:** Writing – review & editing, Methodology, Data curation. **Minghui Tao:** Writing – review & editing, Methodology. **Lunche Wang:** Writing – review & editing, Methodology.

Declaration of competing interest

The authors declare that they have no known competing financial interests or personal relationships that could have appeared to influence the work reported in this paper.

Acknowledgement

This research was funded by Jing-Jin-Ji Regional Integrated Environmental Improvement-National Science and Technology Major Project (Grant No. 2026ZD1210102) and the National Natural Science Foundation of China (Grant No. 42201409).

We acknowledge the European Union's Copernicus Programme and the European Space Agency for providing the Sentinel-5P/TROPOMI Level-2 NO_2 data, the Netherlands Space Office for its contribution to the TROPOMI instrument, and KNMI for developing the operational NO_2 retrieval algorithm and processor.

We also acknowledge the China National Environmental Monitoring Centre (CNEMC) for providing the surface NO_2 concentration and AQI observations. We also acknowledge the NASA Goddard Earth Sciences Data and Information Services Center (GES DISC) for providing the Aura/OMI NO_2 Standard Product and the NASA Land Processes Distributed Active Archive Center (LP DAAC) for providing the MODIS MAIAC AOD product. Finally, we thank the MEIC team at Tsinghua University for developing and providing the MEIC v2.0 emissions inventory.

Appendix A. Supplementary data

Supplementary data to this article can be found online at https://doi.org/10.1016/j.atmosres.2026.109391.

Data availability

All data sets and software used for GEOS-Chem adjoint model simulation are publicly available (https://wiki.seas.harvard.edu/geos-chem/index.php/GEOS-Chem_Adjoint). GEOS-FP data and emission inventories are available from the Harvard Amazon Web Services (AWS) open data repository (https://gcgrid.s3.amazonaws.com/index.html). The MEIC emission data can be freely accessed through the official website (http://meicmodel.org.cn). TROPOMI NO_2 data retrieved by official algorithm are publicly available through the Copernicus Data Space Ecosystem (https://dataspace.copernicus.eu/). TROPOMI NO_2 data retrieved by POMINO algorithm requires a free registration on the platform (https://www.pku-atmos-acm.org/acmProduct.php/). The OMI NO_2 data are publicly available from the NASA Goddard Earth Sciences Data and Information Services Center (GES DISC) at https://disc.gsfc.nasa.gov/datasets/.The MODIS MAIAC AOD dataset is provided by NASA and was accessed and processed via the Google Earth Engine (GEE) platform (https://developers.google.com/earth-engine).

References

Anselin, L., 1995. Local indicators of spatial association—LISA. Geogr. Anal. 27 (2), 93–115. https://doi.org/10.1111/j.1538-4632.1995.tb00338.x.

Atkinson, R., 2000. Atmospheric chemistry of VOCs and NOx. Atmos. Environ. 34 (12), 2063–2101. https://doi.org/10.1016/S1352-2310(99)00460-4.

Bertram, T.H., Thornton, J.A., 2009. Toward a general parameterization of N2O5 reactivity on aqueous particles: the competing effects of particle liquid water, nitrate and chloride. Atmos. Chem. Phys. 9 (21), 8351–8363. https://doi.org/10.5194/acp-9-8351-2009.

Boersma, K.F., Bucsela, E.J., Brinksma, E.J., Gleason, J.F., 2002. OMI Algorithm Theoretical Basis Document, Volume IV: OMI Trace Gas Algorithms: 2. *NO2* (ATBD-OMI-04, Issue). N. D. A. A. Center.

Boersma, K.F., Eskes, H.J., Brinksma, E.J., 2004. Error analysis for tropospheric NO2 retrieval from space. J. Geophys. Res. Atmos. 109 (D4). https://doi.org/10.1029/2003JD003962.

Boersma, K.F., Eskes, H.J., Dirksen, R.J., van der A, R.J., Veefkind, J.P., Stammes, P., Huijnen, V., Kleipool, Q.L., Sneep, M., Claas, J., Leitão, J., Richter, A., Zhou, Y., Brunner, D., 2011. An improved tropospheric NO2 column retrieval algorithm for the ozone monitoring instrument. Atmos. Meas. Tech. 4 (9), 1905–1928. https://doi.org/10.5194/amt-4-1905-2011.

Chimot, J., Veefkind, J.P., de Haan, J.F., Stammes, P., Levelt, P.F., 2019. Minimizing aerosol effects on the OMI tropospheric NO2 retrieval – an improved use of the 477 nm O2 – O2 band and an estimation of the aerosol correction uncertainty. Atmos. Meas. Tech. 12 (1), 491–516. https://doi.org/10.5194/amt-12-491-2019.

Chimot, J., Vlemmix, T., Veefkind, J.P., de Haan, J.F., Levelt, P.F., 2016. Impact of aerosols on the OMI tropospheric NO2 retrievals over industrialized regions: how accurate is the aerosol correction of cloud-free scenes via a simple cloud model? Atmos. Meas. Tech. 9 (2), 359–382. https://doi.org/10.5194/amt-9-359-2016.

Cooper, M., Martin, R.V., Padmanabhan, A., Henze, D.K., 2017. Comparing mass balance and adjoint methods for inverse modeling of nitrogen dioxide columns for global nitrogen oxide emissions. J. Geophys. Res. Atmos. 122 (8), 4718–4734.

Duncan, B.N., Lamsal, L.N., Thompson, A.M., Yoshida, Y., Lu, Z.F., Streets, D.G., Hurwitz, M.M., Pickering, K.E., 2016. A space-based, high-resolution view of notable changes in urban NOx pollution around the world (2005-2014). J. Geophys. Res.-Atmos. 121 (2), 976–996. https://doi.org/10.1002/2015JD024121.

Feng, S., Jiang, F., Wang, H., Wang, H., Ju, W., Shen, Y., Zheng, Y., Wu, Z., Ding, A., 2020. NOx emission changes over China during the COVID-19 epidemic inferred from surface NO2 observations. Geophys. Res. Lett. 47 (19), e2020GL090080. https://doi.org/10.1029/2020GL090080.

Fortems-Cheiney, A., Broquet, G., Potier, E., Berchet, A., Pison, I., Martinez, A., Plauchu, R., Abeed, R., Sicsik-Paré, A., Dufour, G., Coman, A., Savas, D., Siour, G., Eskes, H., Denier van der Gon, H.A.C., Dellaert, S.N.C., 2025. Assessing the ability to quantify the decrease in NOx anthropogenic emissions in 2019 compared to 2005 using OMI and TROPOMI satellite observations. Atmos. Chem. Phys. 25 (12), 6047–6068. https://doi.org/10.5194/acp-25-6047-2025.

Geng, G., Zhang, Q., Martin, R.V., Lin, J., Huo, H., Zheng, B., Wang, S., He, K., 2017. Impact of spatial proxies on the representation of bottom-up emission inventories: a satellite-based analysis. Atmos. Chem. Phys. 17 (6), 4131–4145. https://doi.org/10.5194/acp-17-4131-2017.

Getis, A., Ord, J.K., 1992. The analysis of spatial association by use of distance statistics. Geogr. Anal. 24 (3), 189–206. https://doi.org/10.1111/j.1538-4632.1992.tb00261.x.

Goldberg, D.L., Anenberg, S.C., Kerr, G.H., Mohegh, A., Lu, Z., Streets, D.G., 2021. TROPOMI NO2 in the United States: a detailed look at the annual averages, weekly cycles, effects of temperature, and correlation with surface NO2 concentrations. *Earth's* Future 9 (4), e2020EF001665. https://doi.org/10.1029/2020EF001665.

Guenther, A.B., Jiang, X., Heald, C.L., Sakulyanontvittaya, T., Duhl, T.a., Emmons, L.K., Wang, X., 2012. The model of emissions of gases and aerosols from nature version 2.1 (MEGAN2. 1): an extended and updated framework for modeling biogenic emissions. Geosci. Model Dev. 5 (6), 1471–1492. https://doi.org/10.5194/gmd-5-1471-2012.

Hansen, P.C., 2000. The L-Curve and Its Use in the Numerical Treatment of Inverse Problems. https://api.semanticscholar.org/CorpusID:9665185.

Henze, D.K., Hakami, A., Seinfeld, J.H., 2007. Development of the adjoint of GEOS-Chem. Atmos. Chem. Phys. 7 (9), 2413–2433. https://doi.org/10.5194/acp-7-2413-2007.

Henze, D.K., Seinfeld, J.H., Shindell, D.T., 2009. Inverse modeling and mapping US air quality influences of inorganic PM2.5 precursor emissions using the adjoint of GEOS-

Chem. Atmos. Chem. Phys. 9 (16), 5877–5903. https://doi.org/10.5194/acp-9-5877-2009.
Hsu, C.-H., Henze, D.K., Mizzi, A.P., Harkins, C., Lyu, C., Cooper, O.R., Schwantes, R.H., He, J., Li, M., Wang, S., Stockwell, C.E., Warneke, C., Rollins, A.W., Waxman, E.M., Zuraski, K., Peischl, J., Kondragunta, S., Li, F., Xu, C., McDonald, B.C., 2026. Top-down estimates of U.S. NOx emissions using TEMPO and TROPOMI NO2 remote sensing observations with WRF-Chem/Chem-DART. J. Geophys. Res. Atmos. 131 (2), e2025JD044223. https://doi.org/10.1029/2025JD044223.
Hudman, R.C., Moore, N.E., Mebust, A.K., Martin, R.V., Russell, A.R., Valin, L.C., Cohen, R.C., 2012. Steps towards a mechanistic model of global soil nitric oxide emissions: implementation and space based-constraints. Atmos. Chem. Phys. 12 (16), 7779–7795. https://doi.org/10.5194/acp-12-7779-2012.
Janssens-Maenhout, G., Crippa, M., Guizzardi, D., Dentener, F., Muntean, M., Pouliot, G., Keating, T., Zhang, Q., Kurokawa, J., Wankmüller, R., 2015. HTAP_v2. 2: a mosaic of regional and global emission grid maps for 2008 and 2010 to study hemispheric transport of air pollution. Atmos. Chem. Phys. 15 (19), 11411–11432. https://doi.org/10.5194/acp-15-11411-2015.
Kasibhatla, P., Sherwen, T., Evans, M.J., Carpenter, L.J., Reed, C., Alexander, B., Chen, Q., Sulprizio, M.P., Lee, J.D., Read, K.A., 2018. Global impact of nitrate photolysis in sea-salt aerosol on NOx, OH, and O3 in the marine boundary layer. Atmos. Chem. Phys. 18 (15), 11185–11203. https://doi.org/10.5194/acp-18-11185-2018.
Kharol, S.K., Martin, R.V., Philip, S., Boys, B., Lamsal, L.N., Jerrett, M., Brauer, M., Crouse, D.L., McLinden, C., Burnett, R.T., 2015. Assessment of the magnitude and recent trends in satellite-derived ground-level nitrogen dioxide over North America. Atmos. Environ. 118, 236–245. https://doi.org/10.1016/j.atmosenv.2015.08.011.
Kim, H.C., Lee, P., Judd, L., Pan, L., Lefer, B., 2016. OMI NO2 column densities over north American urban cities: the effect of satellite footprint resolution. Geosci. Model Dev. 9 (3), 1111–1123. https://doi.org/10.5194/gmd-9-1111-2016.
Kong, H., Lin, J., Chen, L., Zhang, Y., Yan, Y., Liu, M., Ni, R., Liu, Z., Weng, H., 2022. Considerable unaccounted local sources of NOx emissions in China revealed from satellite. Environ. Sci. Technol. 56 (11), 7131–7142. https://doi.org/10.1021/acs.est.1c07723.
Kong, Y., Zheng, B., Liu, Y., 2025. Tracking daily NOx emissions from an urban agglomeration based on TROPOMI NO2 and a local ensemble transform Kalman filter. Atmos. Chem. Phys. 25 (11), 5959–5976. https://doi.org/10.5194/acp-25-5959-2025.
Lamsal, L.N., Krotkov, N.A., Vasilkov, A., Marchenko, S., Qin, W., Yang, E.S., Fasnacht, Z., Joiner, J., Choi, S., Haffner, D., Swartz, W.H., Fisher, B., Bucsela, E., 2021. Ozone monitoring Instrument (OMI) Aura nitrogen dioxide standard product version 4.0 with improved surface and cloud treatments. Atmos. Meas. Tech. 14 (1), 455–479. https://doi.org/10.5194/amt-14-455-2021.
Lange, K., Richter, A., Schönhardt, A., Meier, A.C., Bösch, T., Seyler, A., Krause, K., Behrens, L.K., Wittrock, F., Merlaud, A., 2023. Validation of Sentinel-5P TROPOMI tropospheric NO2 products by comparison with NO2 measurements from airborne imaging DOAS, ground-based stationary DOAS, and mobile car DOAS measurements during the S5P-VAL-DE-Ruhr campaign. Atmos. Meas. Tech. 16 (5), 1357–1389. https://doi.org/10.5194/amt-16-1357-2023.
Li, K., Jacob, D.J., Liao, H., Zhu, J., Shah, V., Shen, L., Bates, K.H., Zhang, Q., Zhai, S.X., 2019. A two-pollutant strategy for improving ozone and particulate air quality in China. Nat. Geosci. 12 (11), 906. https://doi.org/10.1038/s41561-019-0464-x.
Li, M., Liu, H., Geng, G., Hong, C., Liu, F., Song, Y., Tong, D., Zheng, B., Cui, H., Man, H., Zhang, Q., He, K., 2017a. Anthropogenic emission inventories in China: a review. Natl. Sci. Rev. 4 (6), 834–866. https://doi.org/10.1093/nsr/nwx150.
Li, M., Zhang, Q., Kurokawa, J.I., Woo, J.H., He, K., Lu, Z., Ohara, T., Song, Y., Streets, D. G., Carmichael, G.R., Cheng, Y., Hong, C., Huo, H., Jiang, X., Kang, S., Liu, F., Su, H., Zheng, B., 2017b. MIX: a mosaic Asian anthropogenic emission inventory under the international collaboration framework of the MICS-Asia and HTAP. Atmos. Chem. Phys. 17 (2), 935–963. https://doi.org/10.5194/acp-17-935-2017.
Li, Y., Wang, T., Wang, Q.g., Li, M., Qu, Y., Wu, H., Xie, M., 2024. Exploring the role of aerosol-ozone interactions on O3 surge and PM2.5 decline during the clean air action period in Eastern China 2014–2020. Atmos. Res. 302, 107294. https://doi.org/10.1016/j.atmosres.2024.107294.
Lin, J.-T., McElroy, M.B., 2010. Impacts of boundary layer mixing on pollutant vertical profiles in the lower troposphere: implications to satellite remote sensing. Atmos. Environ. 44 (14), 1726–1739. https://doi.org/10.1016/j.atmosenv.2010.02.009.
Lin, J.T., Liu, M.Y., Xin, J.Y., Boersma, K.F., Spurr, R., Martin, R., Zhang, Q., 2015. Influence of aerosols and surface reflectance on satellite NO2 retrieval: seasonal and spatial characteristics and implications for NOx emission constraints. Atmos. Chem. Phys. 15 (19), 11217–11241. https://doi.org/10.5194/acp-15-11217-2015.
Lin, J.T., Martin, R.V., Boersma, K.F., Sneep, M., Stammes, P., Spurr, R., Wang, P., Van Roozendael, M., Clémer, K., Irie, H., 2014. Retrieving tropospheric nitrogen dioxide from the ozone monitoring instrument: effects of aerosols, surface reflectance anisotropy, and vertical profile of nitrogen dioxide. Atmos. Chem. Phys. 14 (3), 1441–1461. https://doi.org/10.5194/acp-14-1441-2014.
Lin, S.-J., Rood, R.B., 1996. Multidimensional flux-form semi-Lagrangian transport schemes. Mon. Weather Rev. 124 (9), 2046–2070. https://doi.org/10.1175/1520-0493(1996)124<2046:MFFSLT>2.0.CO;2.
Liu, C., Wang, J., Fang, C., Bai, K., 2025. Deeper NOx emission reductions toward better air quality in the Yangtze River Delta: numerical evidences from NOx and VOCs emissions control measures. Atmos. Res. 321, 108103. https://doi.org/10.1016/j.atmosres.2025.108103.
Liu, H., Jacob, D.J., Bey, I., Yantosca, R.M., 2001. Constraints from ^{210}Pb and ^{7}Be on wet deposition and transport in a global three-dimensional chemical tracer model driven by assimilated meteorological fields. J. Geophys. Res. Atmos. 106 (D11), 12109–12128. https://doi.org/10.1029/2000JD900839.
Liu, M., Lin, J., Kong, H., Boersma, K.F., Eskes, H., Kanaya, Y., He, Q., Tian, X., Qin, K., Xie, P., Spurr, R., Ni, R., Yan, Y., Weng, H., Wang, J., 2020. A new TROPOMI product for tropospheric NO2 columns over East Asia with explicit aerosol corrections. Atmos. Meas. Tech. 13 (8), 4247–4259. https://doi.org/10.5194/amt-13-4247-2020.
Liu, M., Lin, J., Wang, Y., Sun, Y., Zheng, B., Shao, J., Chen, L., Zheng, Y., Chen, J., Fu, T. M., Yan, Y., Zhang, Q., Wu, Z., 2018. Spatiotemporal variability of NO2 and PM2.5 over Eastern China: observational and model analyses with a novel statistical method. Atmos. Chem. Phys. 18 (17), 12933–12952. https://doi.org/10.5194/acp-18-12933-2018.
Long, M.S., Yantosca, R., Nielsen, J.E., Keller, C.A., da Silva, A., Sulprizio, M.P., Pawson, S., Jacob, D.J., 2015. Development of a grid-independent GEOS-Chem chemical transport model (v9-02) as an atmospheric chemistry module for Earth system models. Geosci. Model Dev. 8 (3), 595–602. https://doi.org/10.5194/gmd-8-595-2015.
Lorente, A., Folkert Boersma, K., Yu, H., Dörner, S., Hilboll, A., Richter, A., Liu, M., Lamsal, L.N., Barkley, M., De Smedt, I., Van Roozendael, M., Wang, Y., Wagner, T., Beirle, S., Lin, J.T., Krotkov, N., Stammes, P., Wang, P., Eskes, H.J., Krol, M., 2017. Structural uncertainty in air mass factor calculation for NO2 and HCHO satellite retrievals. Atmos. Meas. Tech. 10 (3), 759–782. https://doi.org/10.5194/amt-10-759-2017.
Lu, Z., Wang, J., Wang, Y., Henze, D.K., Chen, X., Sha, T., Sun, K., 2024. Aggravated surface O3 pollution primarily driven by meteorological variations in China during the 2020 COVID-19 pandemic lockdown period. Atmos. Chem. Phys. 24 (13), 7793–7813. https://doi.org/10.5194/acp-24-7793-2024.
Lucchesi, R., 2013. File Specification for GEOS-5 FP (Forward Processing).
Lyapustin, A., Wang, Y., Laszlo, I., Kahn, R., Korkin, S., Remer, L., Levy, R., Reid, J.S., 2011. Multiangle implementation of atmospheric correction (MAIAC): 2. Aerosol algorithm. J. Geophys. Res. Atmos. 116 (D3). https://doi.org/10.1029/2010JD014986.
Miyazaki, K., Eskes, H., Sudo, K., 2012. Global NO_x emission estimates derived from an assimilation of OMI tropospheric NO_2 columns. Atmos. Chem. Phys. 12 (5), 2263–2288.
Miyazaki, K., Eskes, H., Sudo, K., Boersma, K.F., Bowman, K., Kanaya, Y., 2017. Decadal changes in global surface NOx emissions from multi-constituent satellite data assimilation. Atmos. Chem. Phys. 17 (2), 807–837. https://doi.org/10.5194/acp-17-807-2017.
Moran, P.A.P., 1950. Notes on continuous stochastic phenomena. Biometrika 37 (1/2), 17–23. https://doi.org/10.2307/2332142.
Murray, L. T., Jacob, D. J., Logan, J. A., Hudman, R. C., & Koshak, W. J. (2012). Optimized regional and interannual variability of lightning in a global chemical transport model constrained by LIS/OTD satellite data. J. Geophys. Res. Atmos., 117 (D20). doi:https://doi.org/10.1029/2012JD017934Digital (Object Identifier (DOI).
Ott, L.E., Pickering, K.E., Stenchikov, G.L., Allen, D.J., DeCaria, A.J., Ridley, B., Lin, R.-F., Lang, S., Tao, W.-K., 2010. Production of lightning NOx and its vertical distribution calculated from three-dimensional cloud-scale chemical transport model simulations. J. Geophys. Res. Atmos. 115 (D4). https://doi.org/10.1029/2009JD011880.
Plauchu, R., Fortems-Cheiney, A., Broquet, G., Pison, I., Berchet, A., Potier, E., Dufour, G., Coman, A., Savas, D., Siour, G., Eskes, H., 2024. NOx emissions in France in 2019–2021 as estimated by the high-spatial-resolution assimilation of TROPOMI NO2 observations. Atmos. Chem. Phys. 24 (14), 8139–8163. https://doi.org/10.5194/acp-24-8139-2024.
Prunet, P., Lezeaux, O., Camy-Peyret, C., Thevenon, H., 2020. Analysis of the NO2 tropospheric product from S5P TROPOMI for monitoring pollution at city scale. City Environ. Interact. 8, 100051. https://doi.org/10.1016/j.cacint.2020.100051.
Putman, W.M., Lin, S.-J., 2007. Finite-volume transport on various cubed-sphere grids. J. Comput. Phys. 227 (1), 55–78. https://doi.org/10.1016/j.jcp.2007.07.022.
Qu, Z., Henze, D.K., Capps, S.L., Wang, Y., Xu, X., Wang, J., Keller, M., 2017. Monthly top-down NOx emissions for China (2005–2012): a hybrid inversion method and trend analysis. J. Geophys. Res. Atmos. 122 (8), 4600–4625. https://doi.org/10.1002/2016JD025852.
Qu, Z., Henze, D.K., Theys, N., Wang, J., Wang, W., 2019. Hybrid mass balance/4D-var joint inversion of NOx and SO2 emissions in East Asia. J. Geophys. Res. Atmos. 124 (14), 8203–8224. https://doi.org/10.1029/2018JD030240.
Rijsdijk, P., Eskes, H., Dingemans, A., Boersma, K.F., Sekiya, T., Miyazaki, K., Houweling, S., 2025. Quantifying uncertainties in satellite NO2 superobservations for data assimilation and model evaluation. Geosci. Model Dev. 18 (2), 483–509. https://doi.org/10.5194/gmd-18-483-2025.
Sekiya, T., Miyazaki, K., Eskes, H., Sudo, K., Takigawa, M., Kanaya, Y., 2022. A comparison of the impact of TROPOMI and OMI tropospheric NO2 on global chemical data assimilation. Atmos. Meas. Tech. 15 (6), 1703–1728. https://doi.org/10.5194/amt-15-1703-2022.
Shah, V., Jacob, D.J., Li, K., Silvern, R.F., Zhai, S., Liu, M., Lin, J., Zhang, Q., 2020. Effect of changing NOx lifetime on the seasonality and long-term trends of satellite-observed tropospheric NO2 columns over China. Atmos. Chem. Phys. 20 (3), 1483–1495. https://doi.org/10.5194/acp-20-1483-2020.
Shah, V.R., Jacob, D.J., Dang, R.J., Lamsal, L.N., Strode, S.A., Steenrod, S.D., Boersma, K. F., Eastham, S.D., Fritz, T.M., Thompson, C., Peischl, J., Bourgeois, I., Pollack, I.B., Nault, B.A., Cohen, R.C., Campuzano-Jost, P., Jimenez, J.L., Andersen, S.T., Carpenter, L.J., Evans, M.J., 2023. Nitrogen oxides in the free troposphere: implications for tropospheric oxidants and the interpretation of satellite NO2 measurements. Atmos. Chem. Phys. 23 (2), 1227–1257. https://doi.org/10.5194/acp-23-1227-2023.
van der Werf, G.R., Randerson, J.T., Giglio, L., Van Leeuwen, T.T., Chen, Y., Rogers, B. M., Mu, M., Van Marle, M.J.E., Morton, D.C., Collatz, G.J., 2017. Global fire

emissions estimates during 1997–2016. Earth Syst. Sci. Data 9 (2), 697–720. https://doi.org/10.5194/essd-9-697-2017.

van Geffen, J., Eskes, H., Boersma, K., Maasakkers, J., Veefkind, J., 2022a. TROPOMI ATBD of the Total and Tropospheric NO2 Data Products [Algorithm Theoretical Basis Document, issue 2.4.0](S5P-KNMI-L2-0005-RP).

van Geffen, J., Eskes, H., Compernolle, S., Pinardi, G., Verhoelst, T., Lambert, J.C., Sneep, M., ter Linden, M., Ludewig, A., Boersma, K.F., Veefkind, J.P., 2022b. Sentinel-5P TROPOMI NO2 retrieval: impact of version v2.2 improvements and comparisons with OMI and ground-based data. Atmos. Meas. Tech. 15 (7), 2037–2060. https://doi.org/10.5194/amt-15-2037-2022.

Veefkind, J.P., Aben, I., McMullan, K., Förster, H., de Vries, J., Otter, G., Claas, J., Eskes, H.J., de Haan, J.F., Kleipool, Q., van Weele, M., Hasekamp, O., Hoogeveen, R., Landgraf, J., Snel, R., Tol, P., Ingmann, P., Voors, R., Kruizinga, B., Levelt, P.F., 2012. TROPOMI on the ESA Sentinel-5 precursor: a GMES mission for global observations of the atmospheric composition for climate, air quality and ozone layer applications. Remote Sens. Environ. 120, 70–83. https://doi.org/10.1016/j.rse.2011.09.027.

Wang, Y., Wang, J., Xu, X., Henze, D.K., Qu, Z., Yang, K., 2020. Inverse modeling of SO2 and NOx emissions over China using multisensor satellite data – part 1: formulation and sensitivity analysis. Atmos. Chem. Phys. 20 (11), 6631–6650. https://doi.org/10.5194/acp-20-6631-2020.

Wang, Y., Ying, Q., Hu, J., Zhang, H., 2014. Spatial and temporal variations of six criteria air pollutants in 31 provincial capital cities in China during 2013–2014. Environ. Int. 73, 413–422. https://doi.org/10.1016/j.envint.2014.08.016.

Wang, Y.H., Jacob, D.J., Logan, J.A., 1998. Global simulation of tropospheric O3-NOx-hydrocarbon chemistry: 2. Model evaluation and global ozone budget. J. Geophys. Res. Atmos. 103 (D9), 10727–10755. https://doi.org/10.1029/98JD00158.

Xing, R., Luo, Z., Zhang, W., Xiong, R., Jiang, K., Meng, W., Meng, J., Dai, H., Xue, B., Shen, H., Shen, G., 2024. Household fuel and direct carbon emission disparity in rural China. Environ. Int. 185, 108549. https://doi.org/10.1016/j.envint.2024.108549.

Xiong, J., Wang, Y., Tao, M., Dong, W., Zhou, L., Wang, L., 2026. Vertical structure of the aerosols in the troposphere over the North China Plain: an analysis based on observations and simulations from 2007 to 2022. Atmos. Res. 327, 108348. https://doi.org/10.1016/j.atmosres.2025.108348.

Xu, S., Deng, Z.Y., Zou, B., Zhi, L., 2025. Assessing combined PM2.5-O3 risks in China using a multidimensional hazard-exposure-vulnerability framework (2000−2023). Ecol. Indic. *179*, 114267. https://doi.org/10.1016/j.ecolind.2025.114267.

Yang, L., Hong, S., 2023. Impact of the clean energy structure of building operation on the co-benefits of CO2 and air pollutant emission reductions in Chinese provinces. J. Clean. Prod. 413, 137400. https://doi.org/10.1016/j.jclepro.2023.137400.

Ye, H., Zang, Z., Hu, Y., Liu, N., 2026. Near-real-time inversion of SO_2 emission via coupled three-dimensional variational assimilation and deep learning surrogate framework over China. Atmos. Res. 342, 109151. https://doi.org/10.1016/j.atmosres.2026.109151.

Zhang, Y., Lin, J., Kim, J., Lee, H., Park, J., Hong, H., Van Roozendael, M., Hendrick, F., Wang, T., Wang, P., He, Q., Qin, K., Choi, Y., Kanaya, Y., Xu, J., Xie, P., Tian, X., Zhang, S., Wang, S., Liu, M., 2023. A research product for tropospheric NO2 columns from geostationary environment monitoring spectrometer based on Peking University OMI NO2 algorithm. Atmos. Meas. Tech. 16 (19), 4643–4665. https://doi.org/10.5194/amt-16-4643-2023.